https://doi.org/10.5194/egusphere-2025-3011
Preprint. Discussion started: 1 July 2025

Modeling the combined effects of the 2023 Türkiye-Syria Earthquake and an Atmospheric River event on landslide hazard

Hunter N. Jimenez[1], Erkan Istanbulluoglu[1], Tolga Gorum[2], Thomas A. Stanley[3], Pukar M. Amatya[3], Hakan Tanyas[4], Mehmet C. Demirel[5], Aykut Akgun[6], Deniz Bozkurt[7]

[1]Civil and Environmental Engineering Department, University of Washington, Seattle, WA, USA
[2]Eurasia Institute of Earth Sciences, Istanbul Technical University, Istanbul, Türkiye
[3]NASA Goddard Space Flight Center, Greenbelt, MD, USA
[4]Faculty of Geo-information Science and Earth Observation (ITC), University of Twente, Enschede, The Netherlands
[5]Civil Engineering Department, Istanbul Technical University, Istanbul, Türkiye
[6]Geological Engineering Department, Karadeniz Technical University, Trabzon, Türkiye
[7]Department of Meteorology, University of Valparaíso, Valparaíso, Chile

Correspondence to: Hunter N. Jimenez (hunterjimenez@outlook.com)

Abstract. This study investigates the landslide hazards resulting from the compound effects of the February 6, 2023 Türkiye-Syria earthquakes and a subsequent atmospheric river (AR) event that delivered up to 183 mm of rainfall across the earthquake-impacted region. Using the open-source Landlab modeling toolkit, we integrate global satellite datasets to simulate shallow landslide hazard at a regional scale. Our landslide hazard model incorporates earthquake legacy effects, a seismic driver accounting for post-seismic hillslope weakening, and rainfall drivers into a probabilistic implementation of the infinite slope stability theorem through a Monte Carlo approach. Model validation using landslide inventories and satellite-derived surface change metrics confirms improved performance for rainfall-driven landslide hazards when legacy effects are included. The legacy model reveals an approximately 13° reduction in critical slope angle and identifies high-hazard zones consistent with observed and inferred failures. Additionally, we analyze how the sequence of extreme seismic and rainfall events influences landslide hazard. We find that the scenario where the AR event precedes the earthquakes produces the greatest hazard, with median critical slopes up to 7° lower than other models in high-probability bins (probability of failure, $P(F) > 0.6$) and nearly double the number of grid cells exceeding $P(F) > 0.8$ compared to the next closest scenario. We demonstrate how using historical extreme rainfall records can effectively replicate post-seismic landslide hazard maps that use real-time data, offering a rapid approach for hazard forecasting in tectonically active and climate-sensitive regions.

1 Introduction

Ground shaking from strong earthquakes can trigger coseismic landslides, often concentrated on steep slopes and near hillcrests where shaking is amplified by topography (Meunier et al., 2008; Meunier et al., 2013; Marc et al., 2016). Coseismic landslides mark the beginning of a chain of cascading earthquake hazards (CEHs), including debris flows, mudflows, and sedimentation in streams. Landscapes may remain susceptible to such secondary earthquake hazards for months and even years after the initial seismic event (Fan et al., 2019).

A key element of CEH is the continued supply of sediment from hillslopes after the major shocks. Following earthquakes, hillsides become more susceptible to landslides due to a combination of factors such as topographic change, soil/rock fractures, damage to vegetation, and changes in soil hydrologic properties (Leshchinsky et al., 2021; Xi et al., 2024; Brain et al., 2017). Such "earthquake legacy" effects often lead to a reduction in rainfall thresholds for landslide initiation, resulting in higher landslide rates during the post-seismic period compared to the pre-seismic phase (Lin et al., 2004; Zhang and Zhang, 2017). These high landslide rates persist over varying time windows, ranging from months to years, depending on seismic, climatic, and topographic conditions, as well as the amount of loose coseismic landslide deposits exposed by a given earthquake. (Tanyas et al., 2021a). Elevated landslide rates and sediment exports are generally high in regions with high topographic relief, seasonally varying rainfall, and substantial coseismic deposits (Fan et al., 2019; Tanyaş et al., 2021b). Conversely, extreme rainfall can shorten the period during which the landscape experiences elevated susceptibility by rapidly exporting large amounts of sediments from the earthquake-affected zone (Lenti & Martino, 2013; Brain et al., 2021; Brain et al., 2017).

Many examples of CEHs have been reported in the literature. For example, monsoon rainfalls following the 2015 Gorkha earthquakes produced more landslides than similar rainfalls in the pre-seismic period (Jones et al., 2021; Kincey et al., 2023; Burrows et al., 2023). After the Chi-Chi earthquake in Taiwan, sediment yields peaked above five times the background rates, gradually returning to pre-earthquake levels in six years (Hovius et al., 2011). A decade after the 2008 Wenchuan earthquake, which had a long recovery period due to large amounts of coseismic deposits, about 88% of the deposits remained on hillsides (Francis et al., 2022; Tanyaş et al., 2021a).

As part of CEH, we can also consider flooding, as coseismic deposits may exacerbate flood hazards. Two years after the 2008 Wenchuan earthquake, heavy rainfall remobilized sediments accumulated from coseismic landslides in the foothills and mountain terraces. Aggradation of these sediments in river channels reduced the conveyance capacity of rivers, causing extensive flooding hazards (Hairong et al., 2017; Huang & Fan, 2013; Liu & Yang, 2015).

Some extreme combinations of these factors converged in the aftermath of the Feb 6th 2023 Turkiye-Syria earthquake doublet (Mw 7.8 and Mw 7.5) along the East Anatolian Fault Zone (Fig. 1). This earthquake triggered more than 3,600 coseismic landslides (Görüm et al., 2023). On March 14-15 2023, a rare atmospheric river event caused extreme rainfall in the central part of the earthquake-impacted region, bringing up to 183 mm rain over two days at some locations (Görüm et al., 2025). Extreme rainfall triggered more landslides and debris flows in the source areas, and flooding in downstream

https://doi.org/10.5194/egusphere-2025-3011
Preprint. Discussion started: 1 July 2025

communities, causing a major disruption in earthquake recovery efforts, damage to temporary shelters, and life loss (Görüm et al., 2025).

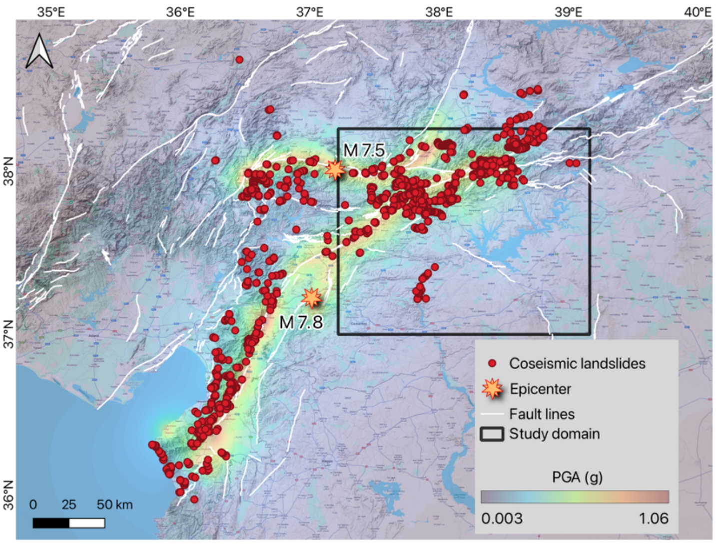

Figure 1: USGS ShakeMap raster composition which consists of PGA resulting from the two major earthquakes of magnitude Mw 7.8 and Mw 7.5 (exclusive of aftershocks) occurring along the East Anatolian fault zone. The coseismic landslide inventory, marked by red circles, is provided by Gorum et al. (2023), while the active faults, indicated by white lines, are mapped by Emre et al., (2013).

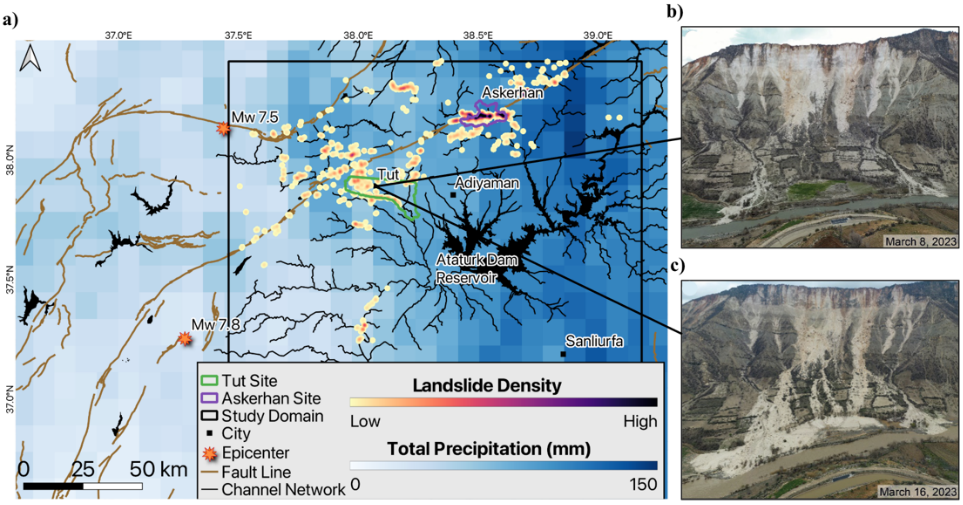

Figure 2: USGS a) NASA's Integrated Multi-satellitE Retrievals for GPM (IMERG) precipitation estimates for March 10-16 2023. This is the initial peak of the atmospheric river event that swept through the central part of the earthquake impacted area, delivering up to 146.4 mm of rainfall over a 7-day span. Photos captured within the town of Tut illustrate the landscape effects of

(b) coseismic driven crown cracking and landsliding and (c) post-seismic storm-driven sedimentation and debris flow (Görüm et al., 2025). Tut and Askerhan sites, where post-seismic landslides were reported, are selected for model validation.

Many earthquake-prone mountainous regions are also increasingly vulnerable to extreme climatic drivers such as intense rainfall, monsoons, or AR. In Türkiye, the frequency and intensity of atmospheric rivers have increased in recent decades specifically during the cold season, particularly in late winter and early spring when snowmelt conditions prevail and soils are already saturated, heightening the risk of runoff-induced hazards (Bozkurt et al. 2021; Görüm et al., 2025). This pattern is not unique to Türkiye - globally, regions like the Pacific coast of the United States, which also face similar seismic hazards, are projected to experience higher AR intensity and frequency (Warner et al., 2015; Wang et al. 2023). Yet, forecasting secondary cascading hazards like post-earthquake landslides remains absent from most earthquake hazard protocols. Although models have begun to link seismic and hydrologic drivers of landslides, they remain limited to research applications in small-scale or case-specific settings (van den Bout et al., 2022; Chen et al., 2023). There is a need to develop regional scalable models that can be rapidly deployed to proactively map landslide hazards resulting from compound effects of seismic and weather extremes.

In this research we formulate such a modeling approach for shallow landslides, and address two main questions First, how can we develop post-seismic landslide hazard maps at regional scales using global data products? Second, how can we model the potential severity of compound seismic and climatic drivers on landslide hazards?

These questions are addressed in the northeastern portion of the earthquake-impacted areas in Turkiye (Fig 2), using the open-source Landlab earth surface modeling framework (Hobley et al., 2017). Global satellite-derived products for rainfall and soil moisture, gridded soil and vegetation parameters are used to inform Landlab. The use of global datasets enables model deployment in data-scarce or rapid-response settings, where local ground measurements may be unavailable. Earthquake legacy effects in lowering rainfall thresholds for landsliding is incorporated with an empirical model, which was developed based on post-seismic rainfall-driven landslide observations from the literature (Xi et al., 2024).

This study includes three groups of analyses based on model parameterizations from gridded soil, vegetation, seismic, lithologic data sets for the region reported in Fig. 2. First, we illustrate the modeled hydrologic response to the March 15 AR event and map post-seismic landslide probability with and without the incorporation of the earthquake legacy effects. These maps are corroborated with observational evidence. Second, we analyze how sequences of extreme seismic and rainfall events influence landslide susceptibility and hazard mapping, highlighting the amplified instability of combined drivers. Finally, we illustrate our method for mapping post-seismic secondary landslide hazards using major storm events (return periods of 5 years or above) from historical IMERG data along with earthquake legacy, which can be adapted in earthquake-prone areas to enhance disaster preparedness. By relying on historical extremes rather than real-time rainfall observations, this approach enables proactive identification of high-risk zones before storms occur, supporting early warning and mitigation efforts.

2 Study site and event context

The model is applied to a study area in the north-central and eastern parts of the earthquake-impacted area, covering the towns of Tut, Adiyaman and Sanliurfa that were impacted from the extreme rainfall event on March 14-16 exacerbated by an AR (Fig. 2). The mountains in the northern part of the study domain mark the highest elevations within the earthquake region, and deliver sediment to the tributaries of the Euphrates River and the Atatürk Dam Reservoir. These physiographic differences are accompanied by considerable climatic variability across the region.

Climate varies over the earthquake-impacted region, from cold and arid in the north to temperate in the south (Fig. 1). Coastal mountains in the south can get annual precipitation as high as 1,200 mm where elevations rapidly rise to 1,700 m. The dry season is from June through September, during which the region overall receives <10 mm per month of rainfall. Consistent with this precipitation gradient, vegetation cover changes from evergreen-mixed forests in the south to seasonal grassland and desert shrubs (i.e., rangeland) to the north of the earthquake impacted area. In our modeling domain, annual precipitation is ~700 mm around Kahramanmaras and Adiyaman, and less than 400 mm in Malatya.

This region presents a rare instance of a powerful seismic event followed by an AR. The earthquakes (Mw 7.8 and Mw 7.5, 9-hours apart) occurred on nearly vertical strike-slip faults, impacting an area of >90,000 km^2 at peak ground acceleration (PGA) up to 1.06 g. On different fault segments surface rupture of the earthquake caused vertical offsets in the 0.5m – 1.7m range, and horizontal ground offsets in the 3.4 m to 6.7 m range (Meng et al., 2024).

Roughly 15% of the region has local slopes greater than 20º. Combined with steep topography and relatively wet conditions, the earthquake sequence triggered more than 3,600 coseismic landslides (Fig. 1) mapped and described by Gorum et al. (2023). Based on their observations, most coseismic landslides consisted of hillside colluvium and rock, including rotational slumps, whereas pure rock falls were observed on steep slopes and near hill crests. More than 70% of landslides occurred within a 10 km (20 km)-wide zone around the faults. Except for some slow-moving slides, landslides were found in 20º-45º slopes and the PGA range of 0.2-0.7. With respect to aspect, landslides were more frequent on southeast- and southwest-facing slopes compared to northern aspects, while the aspect distribution of the landscape is only slightly skewed toward the south. Many landslides were also triggered by surface rupture that crossed through the mountainous terrain, mostly in the north (mountains of Kahramanmaras, Adiyaman) within our modeling domain (Fig. 2) and formed many pervasive tension cracks along the rupture zones. These cracks make the landscape susceptible to future post-seismic landslides, mostly along limestone units (Gorum et al., 2023).

We selected subcatchments in Tut and Askerhan for model validation due to documented landslides during both coseismic and postseismic periods (Görüm et al., 2025; Fig. 2). The Tut subcatchment was selected because it received the highest rainfall from the March 14-15 AR event, which was steered toward the earthquake-affected region by prevailing atmospheric circulation patterns (Görüm et al., 2025). Hillslopes in this region were already substantially more prone to failure due to ground disturbance from the earthquake sequence. The Askerhan subcatchment, located between the Çat Dam and the Atatürk Reservoir, experienced strong ground motion from a ruptured fault line running through its center (Fig. 2), which would amplify the legacy effects of the earthquake. Together, these two subcatchments contain nearly 46% of the observed coseismic landslide inventory within the study domain (a total of 1,087 mapped landslides). The Tut and Askerhan subcatchments are not closed watersheds, with both channel networks expanding to the northeast of their respective locations (Fig. 2).

3 Methods

In this research, we used the Landlab earth surface modeling toolkit to model landslide risk with climatic and seismic drivers. Landlab is an open-source, Python-based framework that provides flexible model customization and coupling (Barnhart et al., 2020; Hobley et al., 2017) for earth surface and near surface processes. Landlab offers grid class objects (called ModelGrid) and a suite of pre-built process modeling components. Landlab utilities are used to handle data creation, management, and interoperability among process components. Spatial data from external sources and modeled state variables can be attached to the elements of a grid (e.g., node, edge) as Landlab data fields. Components are coupled by writing a Landlab “model driver” Python script. The model driver developed for this study couples soil moisture and landslide probability components of Landlab with some limited adaptation described in this section. The model driver and data for a sample model run is available in the data section.

In this study we used the RasterModelGrid object of Landlab to store and use the Digital Elevation Model (DEM), and hydrologic and geotechnical parameters related to soil and vegetation, obtained from the global gridded data sources described in section 4. A soil water balance model is developed by combining Landlab’s Radiation, PotentialEvapotranspiration, and SoilMoisture components. This model is used to calculate daily water balance and obtain recharge for a 7-day period, composed of 5 days before and 2 days after the peak daily rainfall within a storm event. Local recharge (r) calculated at each mode element is routed downstream to estimate an upslope-average recharge rate, R, which is used in the LandslideProbability component as described below. Note that all model components of Landlab use compound words with capitalized first letters of each word.

https://doi.org/10.5194/egusphere-2025-3011
Preprint. Discussion started: 1 July 2025

3.1 Landslide hazard model

In this study, we delineate landslide hazard with shallow landslide probability for a given rainfall event or seismic activity. For this purpose, we describe the various uses of the probabilistic application of the infinite slope stability model in Landlab in the following order: 1) Landlab LandslideProbability component and its implementation for rainfall-driven, post-seismic landslides under the influence of earthquake legacy; 2) probabilistic modeling of coseismic landslides given wetter soil conditions, representing the case which an extreme rainfall event precedes a powerful earthquake. Models are run at a 90 m grid resolution to make a regional application computationally feasible. However, to incorporate local slope variability within grid cells, we resample a 30 m slope grid to the model resolution using the min, median, and max values within each 90 m cell to parameterize the triangular distribution. This method is preferred to retain distributed information on slopes, which is critical for landslide initiation in this regional application.

3.1.1 LandslideProbability component

For the probabilistic modeling of rainfall-driven post-seismic landslides we used the Landlab's landslide probability component. This component is based on a Monte Carlo solution of the infinite slope stability equation derived from the Mohr-Coulomb failure law. The infinite slope stability equation predicts the factor-of-safety (FS) of an infinite plane from the ratio of the stabilizing forces of cohesion and friction to the destabilizing forces of gravity and pore water pressure (Hammond et al., 1992; Wu and Sidle, 1995). This model allows the calculation of factor-of-safety as follows (Pack et al., 1998):

$$\mathrm{FS} = \frac{C^*}{\sin\alpha} + \frac{\cos\alpha\ \tan\phi\left(1 - R_w\frac{\rho_w}{\rho_s}\right)}{\sin\alpha} \tag{1a}$$

$$C^* = \frac{C_t}{h_s \rho_s g} \tag{1b}$$

$$R_w = \frac{h_w}{h_s} = \min\left(\frac{Ra}{T\sin\alpha}, 1\right) \tag{1c}$$

where C_t is combined cohesion for root, C_r, and hillslope materials (soil and rock) C_s (Pa) such that $C_t = C_r + C_s$; h_s is the perpendicular depth of soil over the bedrock or the failure plane (m); ρ_s and ρ_w are saturated soil bulk density and water density (kg m^{-1}), g is the acceleration due to gravity (m s^{-2}), α is the slope angle of the ground, and ϕ is the internal friction angle. C^* is the dimensionless cohesion representing the relative contribution of geologic cohesive forces to slope stability (Pack et al., 1998). R_w represents the local relative wetness, defined as the ratio of subsurface flow depth, flowing parallel to the surface, to soil thickness. R_w follows the simple kinematic-wave representation of steady-state subsurface flow following TOPMODEL (Beven and Kirby, 1979). R is upslope averaged recharge at each model element calculated as $R = (D\ l_c\ a^{-1})$, where the product of local recharge (D, m d^{-1}) and cell length (l_c, m) are summed for the cells upslope of specific catchment area (a, m). Surface water is routed using an 8-direction flow director, allowing excess surface water to move downslope to adjacent cells (Baum et al., 2002). $T\sin\alpha$ is the subsurface flow capacity of the soil layer. In this equation, T represents soil transmissivity (i.e., depth integrated hydraulic conductivity, m^2 d^{-1}) and is derived as the product of the soil saturated hydraulic conductivity (K_s) and h_s for each cell (Strauch et al., 2018). When uncertainty is introduced in the soil and hydrologic parameters of this equation, probability of slope failures is:

$$\mathrm{P(FS \leq 1)} = \int_0^{FS=1} f(FS)dFS \qquad (2)$$

Landlab uses a Monte Carlo approach to calculate landslide probability at each model element by sampling stochastic model parameters, C_t, ϕ, h_s, and T from their respective triangular distributions, and R from the log-normal distribution, parameterized for each model grid cell. Gridded soil, lithology, and vegetation data products are utilized to infer the mode parameters of the triangular distribution for C_t, C_s, h_s, and T. The triangular distributions of h_s, K_s, and T are assumed to be left-skewed distributions commonly observed for these soil features, with ranges derived from previous literature (e.g., Hammond et al., 1992). In contrast, minimum and maximum ϕ were calculated to generate right-skewed triangular distributions (e.g., Table 5.5 in Hammond et al., 1992, and Table 5.2 in Selby, 1993).

All probability distributions used in the Monte Carlo model are parameterized locally at each grid cell. For recharge, we use the log-normal distribution, where the local mean and standard deviation are taken as R and 30% of R, respectively. To parameterize C_t, we first identified the min, max, and mode values for C_r, as well as the mode value of C_s, from previous literature (Strauch et al., 2018; Xi et al., 2024). Triangular distribution parameters for C_t are obtained using ±30% of the mode C_s values: 70% of the mode C_s was added to the min C_r and 130% of the mode C_s was added to the max C_r. Triangular distribution parameters for local slope are obtained from 30 m grid cells contained within a 90 m resampled grid.

In the Monte Carlo solution of landslide probability we used 2500 iterations (N), which is more than the sufficient range of 700 (Malkawi et al., 2000) to > 1200 (Abbaszadeh et al., 2011) found in previous literature. This method generates unique model parameters chosen from a triangular distribution of the random variables at each node of the model cell and calculates relative wetness (Eq. 1c) and FS (Eq. 1a) for each iteration. $\mathrm{P(FS \leq 1)}$ is then calculated as the ratio of number of times FS is less than or equal to 1, $\mathrm{n(FS \leq 1)}$, to the total number of iterations, N.

3.2 Earthquake legacy effects and Newmark analysis

Earthquakes influence landslides through two mechanisms: seismic shaking that immediately triggers failure and post-seismic "legacy effects" which introduce weakening of hillslopes that persists over time, increasing susceptibility to future failures. Earthquake legacy on landslide hazard in the post-seismic phase is introduced based on a linear model proposed by Xi and Tanyas (2024) where reduction of shear strength (RSS) at landslide locations was linearly related to PGA as: $RSS = 0.52 + 0.2\ PGA$. This equation was developed using coseismic landslides observed at the 2008 Wenchuan, China earthquake, but later corroborated with observations from coseismic landslides in 2015 Gorkha and 2018 Palu earthquakes (Xi et al., 2024). In our simplistic model, RSS is only absorbed by the combined cohesion and introduced as a multiplier to C^* in Eq. (1b):

$$\mathrm{C}^* = \frac{\mathrm{C_t}(1-(0.52+0.2\mathrm{PGA})}{\mathrm{h_s}\rho_\mathrm{s}\mathrm{g}} \tag{3}$$

We characterize the seismic slope activity according to the Newmark analysis (Newmark, 1965). The Newmark analysis relates coseismic sliding mass to a rigid block on an inclined plane, where permanent downslope displacement is initiated at the block's critical acceleration. In this case, critical acceleration, a_c (m s^{-2}), is defined as the seismic acceleration required to overcome basal shear resistance between the block and the plane, and can be approximated with Eq. (4):

$$a_c = (FS-1)gsin\alpha \tag{4}$$

where FS is the factor-of-safety, g is the gravitational constant 9.81 m s^{-2}, and α is the slope angle (Newmark, 1965). With spatial coverage of the peak ground acceleration (PGA) measured during the coseismic period (i.e., USGS ShakeMap, USGS 2023a; USGS 2023b) and expressed as a fraction of g, our initial equation is rearranged, by replacing a_c divided by g with observed PGA and solving for FS, to approximate a minimum FS value required for a stable hillslope during an earthquake.

$$\tau_{PGA} = \frac{PGA}{sin\alpha} + 1 \tag{5}$$

Thus, if the FS of a hillslope right before the earthquake is greater than τ_{PGA}, then the slope is expected to remain stable. PGA:sinα can be viewed as the additional proportion of resisting forces to driving forces required for slopes to remain stable during an earthquake (Zang et al., 2020). Extreme rainfall that precedes an earthquake could exacerbate the extent and magnitude of coseismic landslides. To calculate the probability of coseismic landslides with $R > 0$, we now solve the probabilistic Eq. (2) with an upper limit of τ_{PGA} as

$$\mathrm{P}\left(\mathrm{FS} \leq \tau_{PGA} = \frac{PGA}{sin\alpha} + 1\right) = \int_0^{FS=\tau_{PGA}} f(FS)dFS \tag{6}$$

note that R does not necessarily indicate that an earthquake happens during a rainfall event, but sometime during or after rainfall while recharge to subsurface flow continues.

3.3 Delineating Rainfall-Driven Landslides

The performance of a landslide hazard model is based on its ability to delineate existing mapped landslides**.** While a coseismic landslide inventory of mapped initiation points and landslide polygons exists in the literature for the February 2023 earthquake doublet (Görüm et al., 2023), it does not capture rainfall-driven landslides that occurred in the following weeks. To address this, we develop a landslide inventory that includes both observed coseismic and inferred rainfall-driven failures, focusing on two sites (Fig. 2) where extensive landslides were reported. Specifically, we use surface reflectance change methods to identify additional landslides triggered during the March 14–15, 2023 AR event. The existing inventory is used to corroborate the potential landslides identified with the method presented here.

To create a rapid observed landslide inventory that includes rainfall-driven debris flow for model validation, we use an improved version of bare soil index (BSI) that effectively links the spectral response of the ground before and after the events, and is scaled to improve interpretation (Ariza et al., 2021). Traditional BSI, a numerical index that combines blue, red, near infrared and short-wave infrared spectral bands to discriminate bare soil (Diek et al., 2017; Chen et al., 2004), can be insufficient in the study region due to naturally sparse vegetation and exposed soils, which may be misclassified as landslides. To address this limitation, we used BSI difference (dBSI) to map landslides by subtracting the post-event values of BSI from the initial values (Equation 7; Ariza et al., 2021). Results are scaled by a factor of 1000 to facilitate clearer interpretation and range detection (Ariza et al., 2021). Areas with values that reflect the presence of landsliding will appear with negative values.

$$\text{dBSI} = 1000(BSI_{pre} - BSI_{post}) \tag{7}$$

Sentinel-2 imagery (10 m) for June 2022 and June 2023 are used to visualize surface conditions before and after the March 2023 event, respectively. Sentinel-2 was selected over higher-resolution alternatives due to its open-access availability and consistent temporal coverage. June was selected to minimize cloud and snow cover biases common in mountainous regions during spring, while ensuring sufficient vegetation coverage to reduce misclassification of naturally exposed soils or dead vegetation as landslides.

Due to the variability in surface cover, soil, vegetation, and aspect across our large study area (> 24,000 km²), reflectance-based landslide classification presents limitations. To improve reliability, we limited model evaluation to smaller subcatchments (Tut and Askerhan; Fig. 2) where higher P(F) values and observed landslides were concentrated during the AR event (Görüm et al., 2025). To minimize the misclassification of local phenomena, such as bright surfaces (e.g., sunlit rock or soil) and year-to-year NDVI/BSI change, as landslides, we use the second percentile values of dBSI as a conservative threshold. A slope threshold of 15° and steeper is used to filter out landslide classification on gentle slopes. All pixels remaining after thresholding and slope filtering are included in the inventory. We did not explicitly filter out mapped coseismic landslides, as many slopes that failed during shaking were likely already near failure and may have also been susceptible to intense rainfall. While the legacy model is not designed to capture shaking-induced failures directly, it incorporates seismic forcing through reduced shear strength, representing the weakened state of the landscape following the earthquake.

ROC curves are constructed from true and false positive rates from comparisons between inferred landslide locations and modeled landslide hazard for slopes >15°, based on varying P(F) thresholds (Strauch et al., 2018; Fawcett, 2006). For comparison of P(F) with observed landslide inventory cells, we randomly sampled an equal number of non-landslide grid cells outside mapped debris avalanches that were constrained to the same slope thresholds (15°) as our inferred landslides. This method alleviates bias introduced by class imbalance, which could inflate model accuracy by over-representing non-landslide areas. More effective models will exhibit a curve toward the upper left of the plot, while a 1:1 line represents a trivial model that assigns stable and unstable classifications randomly. The area under the ROC curve (AUC) is generally used to signify the model performance for identifying landslide and non-landslide points, representing the probability of correctly ranking a randomly selected landslide and non-landslide pair.

3.4 Recharge

Daily recharge, *D*, is modeled with Landlab's SoilMosture component (Nudurupati et al., 2023), which tracks soil moisture using a single-layer, depth-averaged root zone water balance model, driven by daily rainfall pulses and potential evapotranspiration (*PET*). Recharge in this context refers to the root zone leakage rate to the subsurface water table from rainfall after evapotranspiration losses and changes in soil storage within the root zone (Laio et al., 2001; Equation 8). The continuity of soil water in the root-zone is modeled by:

$$nZ_r \frac{ds}{dt} = P_e - ET_a(s) - D(s) \qquad (8)$$

where n is soil porosity, Z_r is effective root depth, s is relative saturation (volumetric soil moisture content, θ, normalized by n), P_e is effective rainfall that directly increase soil moisture, ET_a is the actual rate of evapotranspiration, and D is leakage. Effective rainfall (P_e) is the portion of total rainfall (P) that remains after accounting for losses from initial abstraction (I_a) and runoff (Q), and is introduced in the soil column as a pulse, $P_e = P - I_a - Q$. Surface runoff is computed via the conceptual Curve-Number model (e.g., Steenhuis et al., 1995):

$$Q = \frac{(P-I_a)^2}{(P-I_a+S_{max})} \qquad (9)$$

where S_{max} is the maximum retention parameter prior to a storm, which is taken as the available pore space within the root zone, $S_{max}=(n - \theta)\,Z_r$. We assumed $I_a = 0.05\,S_{max}$, consistent with dry landscape conditions (Lim et al., 2006). This formulation has been extensively tested and used for rangeland surface hydrology.

The resulting storm infiltration depth serves as the infiltration input to the soil moisture model. Potential Evapotranspiration (*PET*) is estimated using the Priestley-Taylor method, with net radiation calculated using the Landlab Radiation component which follows guidelines established by ASCE-EWRI (2005). Daily *PET* calculations incorporate latitude, albedo, day-of-year, and daily minimum and maximum temperatures (T_{min}, T_{max}, respectively. The rate of ET_a is a linear function of evapotranspiration efficiency β [0-1] that scales ET_a between PET of vegetated and bare soil fractions as a function of θ, until θ reaches the wilting point, θ_{wp} (e.g., Laio et al., 2001). *D(s)* remains as a function of the rate of soil moisture drawdown following the precipitation event, which is modeled analytically following Laio et al. (2001), assuming unit hydraulic head gradient and exponential decay of hydraulic conductivity between saturation ($D = K_{sat}$) and field capacity ($D = 0$). While IMERG precipitation (10 km) drives the input, the SoilMoisture component refines the spatial resolution of saturated soils to the native resolution (90 m) of vegetation and soil parameters used to run the model, offering a more granular representation of recharge and runoff rates.

For each peak rainfall event, the soil moisture model is run for 7 days, starting 5 days leading up to observed peak rainfall (inclusive) and two days after the event. For each event, soil moisture was initialized at ~35% of plant-available moisture on day 1, calculated as: $\theta_i = (0.35\ (\theta_{fc} - \theta_{wp}) + \theta_{wp})$ divided by n, where θ_{fc} is field capacity, θ_{wp} is wilting point, and n is soil porosity. After calculating the upslope average recharge (R) we perform a temporal reduction by looping through daily R fields over the 7-day window and returning the maximum R (mm d^{-1}) at each cell. For our historical analysis, we further extend this approach by applying a spatial reduction across multiple past events, identifying the highest recharge rate observed at each cell over all events. This approach helps delineate the areas most susceptible to saturation under the worst-case precipitation scenarios that have been observed, providing a valuable indicator of slope instability.

4 Data sources and model experiments

We use a variety of ground- and satellite-based remote sensing products to effectively model secondary landslide hazards. Below, these data sources are discussed in two groups: land surface and soils; and model forcing (climate and seismic). A grid resolution of 90 m is used over a model domain of nearly 25,000 km^2 (Fig. 2). The Raster Model Grid (RMG) class generates a structured grid that spans the model domain. Spatial model parameters and forcing data, prepared during preprocessing outside of Landlab as ascii files, are loaded onto the grid. These data are stored at the grid nodes (center points of the cells) as Landlab data fields. Data reprojection and boundary filtering to match the resolution and extent of the study domain were performed using the raster and vector geospatial translator library GDAL (GDAL/OGR 2024). Fig. 3 shows examples of these products and their sources, demonstrating how the gridded data are integrated into Landlab as fields that can be used for computation. These parameters were used directly, without any calibration, except for the anisotropy multiplier used to estimate lateral saturated hydraulic conductivity. Model input parameters are summarized in Table 1.

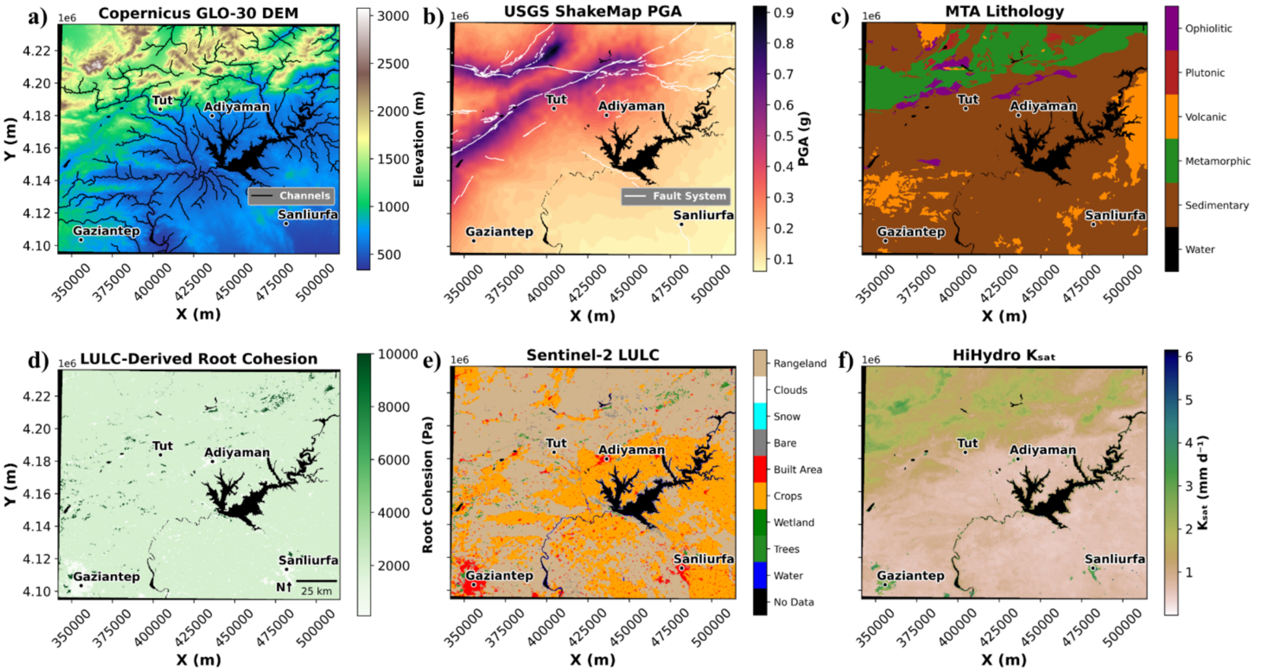

Figure 3. Illustration of model-data integration of remote sensing products into Landlab as fields: a) Copernicus GLO-30 DEM, b) USGS ShakeMap PGA, c) ESRI Sentinel-2 land use/land cover map, d) root cohesion derived from LULC in panel (c) using literature derived values (Strauch et al., 2018), e) MTA geologic map, and f) HiHydro K_{sat}

4.1 Land surface and soils data

We employed the Copernicus GLO-30 DEM for elevation, with values ranging from > 3,000 m in the northern mountain ranges to < 500 m in the southern plains, over a distance of roughly 60 km. At high elevations ($Z \geq 1{,}200$ m), 46% of slopes exceed 15°, which is approximately the threshold slope for landsliding of saturated sand. We use Sentinel-2 Land Use Land Cover (LULC) to assign vegetation types and their associated root cohesion values as reported in Strauch et al. (2018; Fig. 3), as well as plant functional type (tree, shrub, grass). Rangeland LULC, dominated by grass and shrub species, is prevalent in the upland region where landslides are observed. In contrast, herbaceous cover, such as grass and cultivated crops, dominates the lowland region. We use 1:500,000 geological vector maps of Türkiye (MTA, 2002) to characterize local lithology (Fig. 3). We assigned cohesion and soil internal friction angle couples to each lithologic unit based on values reported in the literature for similar lithologies (Xi et al., 2024). Root cohesion is primarily associated with rangeland and herbaceous cover, which generally exhibit a modal cohesive strength of 2-4 kPa, with small pockets of tree cover providing additional resistance. Sedimentary and metamorphic cover dominates the geologic framework of the study area. Following lithologic unit cohesion tables provided by Xi et al. (2024) for the Himalayan belt, we assign cohesion values of 14.4 kPa for

https://doi.org/10.5194/egusphere-2025-3011
Preprint. Discussion started: 1 July 2025

sedimentary units (e.g., basin fill) and 38 kPa for metamorphic units (e.g., gneiss). As a result, total cohesion in the model is primarily influenced by contributions from rock strength.

Soil thickness was defined using SoilGrids data for absolute depth to bedrock. We enhanced our soil thickness dataset for high-elevation areas by applying an elevation-dependent linear relationship in high-slope regions (>15%), capturing the tendency for thinner soils at higher altitudes due to reduced accumulation and increased erosion. Applying these additional criteria provide soil thickness values in the 0.3-2.0 m range from low to high elevations. Leaf area index (LAI) used by the soil moisture model is obtained from NASA's MODIS (Moderate Resolution Imaging Spectroradiometer). Soil saturated hydraulic conductivity (K_{sat}), wilting point, field capacity, saturated water content (or porosity) and texture classifications were defined using the FutureWater HiHydro dataset. Following the observations of Assouline and Or (2006), gridded K_{sat} values were multiplied by 10 to account for anisotropy in lateral flow, with a minimum value set to 0.5 m d^{-1} to ensure realistic hydraulic conductivity estimates. The soil textural distribution is characterized by two dominant types: medium soil texture in the uplands and fine soil texture in the lowlands, which correspond with the metamorphic and sedimentary lithologic types, respectively (Görüm et al., 2023). Upland versus lowland differentials in LULC and soil texture lead to differences in soil water parameters such as the saturated hydraulic conductivity (Fig. 3).

4.2 Model forcing data

As for the hydrometeorological variables we use IMERG version 7, which estimates precipitation over a majority of the Earth's surface. Daily aggregated minimum (T_{min}) and maximum (T_{max}) temperatures across the domain were derived from ERA-5 temperature fields. *PGA* was retrieved from the USGS ShakeMap (USGS 2023a, 2023b). *PGA* values are combined using the maximum values from the two major earthquakes to create a composite map of the strongest ground motion (Fig. 3). Cells at high elevations ($Z \geq 1200$m) experienced an average *PGA* of 0.4 g, and up to 0.9 g adjacent to the fault system. The soil and water density terms in Eq. (1a) were assigned a constant value of 2,000 and 1,000 kg m^{-3}, respectively (Pack et al., 2005). The factor of safety has been found to be largely unaffected to soil density (Hammond et al., 1992; Lepore et al., 2013).

4.3 Model experiments

We use a series of targeted experiments to explore how the landscape responds to compound seismic and climatic drivers. In Section 5.1, we illustrate the modeled hydrologic response to the March 14–15 AR event. Section 5.2 validates modeled landslide probabilities using an inventory of observed coseismic and inferred rainfall-driven landslides (Section 3.3). Section 5.3 compares probabilistic landslide hazard maps generated with and without earthquake legacy effects. Section 5.4 explores how sequences of extreme seismic and rainfall events influence landslide susceptibility and hazard mapping. Finally, in Section 5.5, we demonstrate an approach for identifying post-seismic landslide hazards using historical IMERG data, combined with legacy effects. This provides a practical method for rapid disaster preparedness in earthquake-prone regions.

https://doi.org/10.5194/egusphere-2025-3011
Preprint. Discussion started: 1 July 2025

405 **Table 1. Remote sensing and other hybrid data (e.g. field gauges, models) used to characterize land surface, soils, and model forcing parameters (e.g. precipitation, PGA).**

Type	Variable	Source	Resolution
I	Elevation	Copernicus GLO-30 DEM	30 m
	Land use/land cover	ESRI Sentinel-2 LULC	10 m
	Lithology	Türkiye General Directorate of Mineral Research and Exploration (MTA) geologic map series	Vector
	Surface reflectance	Harmonized Sentinel-2 Surface Reflectance	10 m
	Leaf area index	NASA MODIS	500 m
II	Soil thickness (depth to bedrock)	ISRIC SoilGrids	250 m
	Saturated hydraulic conductivity (0-30 cm)	FutureWater HiHydro	250 m
	Wilting point (0-30 cm)	FutureWater HiHydro	250 m
	Field capacity (0-30 cm)	FutureWater HiHydro	250 m
	Saturated water content (0-30 cm)	FutureWater HiHydro	250 m
	Soil texture (0-30 cm)	FutureWater HiHydro	250 m
	Top layer soil moisture (0-5 cm)	NASA SMAP-L4	11000 m
III	Precipitation	NASA IMERG v7	11132 m
	Air temperature (2 m)	ECMWF ERA5 Atmospheric Reanalysis	27830 m
	Peak ground acceleration	USGS ShakeMap	Vector

Types: I - Land surface, II - Soils, III - Model forcing

5. Results

5.1 Hydrologic response to March 14-15, 2023 Atmospheric River (AR)

Modeled land surface hydrology for the study region, including spatial averages of model forcing and hydrologic fluxes during the March 14-15 AR event, is summarized in Figs. 4a and 4b. The spatial mean rainfall steadily increased from March 13 and peaked at just over 35 mm d^{-1} on March 14 (Fig. 4a). In the days leading up to the AR, both the maximum air temperature and the difference between maximum and minimum temperatures decreased (Fig. 4a), reflecting the natural storm conditions (e.g., Dai et al., 1999). The convergence of these temperatures suggests increased cloud cover and cooler conditions, before the onset of rainfall on March 12. Due to the southeast to northwest trajectory of the AR event and orographic lift (Görüm et al., 2025), the northeastern part of the domain experienced significantly higher cumulative rainfall than the average rainfall, with some IMERG cells reporting cumulative 7-day precipitation as high as 145 mm (Fig. 4c). Within the study domain, max peak daily rainfall observed by IMERG during the AR event was 104.6 mm d^{-1}, which corresponds to an approximate return period of 1 in 5 years (Fig. 8b). While IMERG slightly underestimates peak daily rainfall compared to rain gauge stations and ERA5 reanalysis at some locations, its spatial distribution aligns well with the observed AR core and areas with documented rainfall-induced impacts, such as Tut and Askerhan (Görüm et al., 2025).

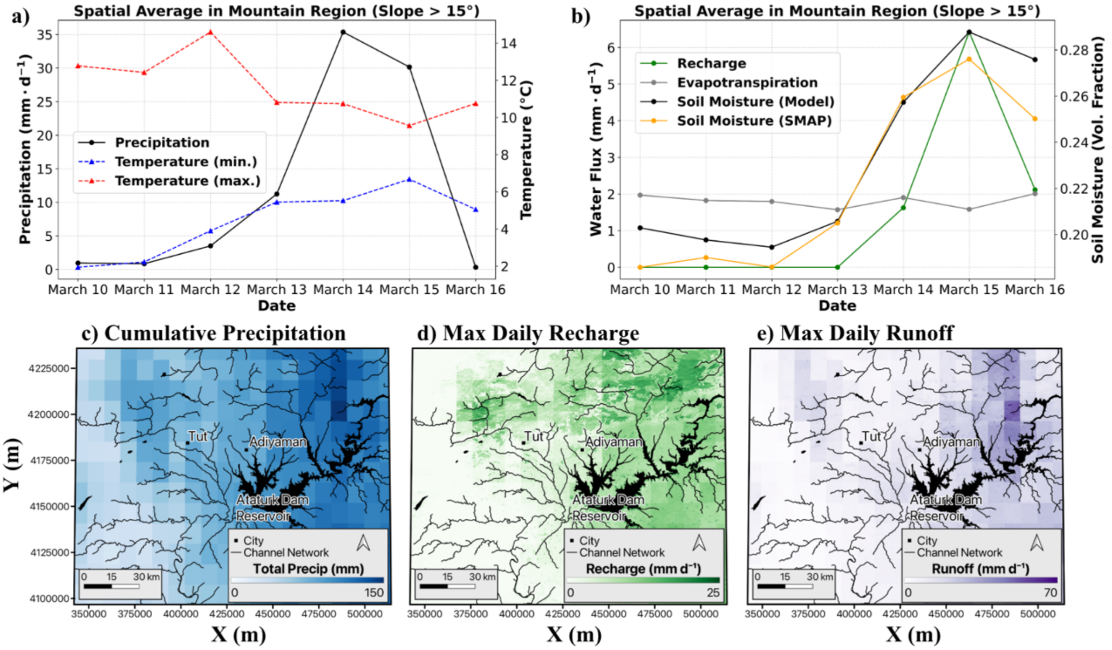

Figure 4. Landlab land surface model response to the March 14-15 AR event: (a) Spatial averages of meteorological forcing of March 10-16 including IMERG precipitation and ERA5 temperature time series. (b) Modeled local recharge, soil moisture, and

evapotranspiration as well as SMAP L4 soil moisture observations. (c) Cumulative IMERG precipitation of the 7-day period, (d) and (e) modeled spatial maximum daily upslope average recharge (*R*) and local runoff (*Q*). Time series are spatial averages of the domain filtered for slopes >15° to report conditions in the mountainous regions. Max daily *R* and *Q* fields are Landlab outputs that are produced from combining the maximum values from the 7 daily response maps to create a composite map of the wettest conditions.

We used soil moisture data from SMAP L-4 satellite derived-product to compare with the modeled soil moisture for the top 30 cm soil depth averaged over slopes >15° (Fig 4b). SMAP surface soil moisture estimates represent the vertical average of the top 5 cm of the soil layer. Both modeled and SMAP soil moisture show consistent values with each other especially during the storm, as they rise in tandem with rainfall to similar levels with a roughly 1-day lag. This lag in soil saturation may be due to factors like interception, infiltration and redistribution. Similar to soil moisture, a rise in recharge begins on March 14 at a small spatially averaged value (< 2 mm d^{-1}) that grows to greater than 6 mm d^{-1} on March 15. This nonlinear growth suggests that the majority of the landscape that sustained heavy rainfall started to experience soil moisture levels above the field capacity that resulted in leakage from the conceptual root-zone of the model. Evapotranspiration (*ET*) losses trended around 2 mm d^{-1}, which is indicative of the cloudy spring-time conditions. Although this value is small, modeling *ET* is necessary to avoid overestimation of recharge, and allows more realistic closure to the root-zone water balance.

Composite maps of maximum daily rates, spanning the 7-day analysis period, report spatial average values of 13.3 and 5.7 mm d^{-1} for local runoff and recharge, respectively. Over the 7-day analysis period, the average cumulative precipitation, runoff, and recharge were 82.0 mm, 21.3 mm, and 8.5 mm, respectively. This indicates that approximately 63% of the total precipitation input was used to increase soil saturation and sustain *ET*. Notably, the average recharge over the entire domain is smaller than the recharge observed in the mountainous region (Fig. 4b), as lower elevations did not receive as much rainfall, and soils had lower K_{sat} and porosity. *R* rates reached up to 27.3 mm d^{-1} on March 14, 2023 and were generally concentrated in soils within the Tut and Askerhan-Çelikhan regions and northeastern mountains. *Q* rates were modeled to reach 69.1 mm d^{-1} on March 14, occurring near and upstream of the saturated Tut, Askerhan-Çelikhan region, and city of Adiyaman, which was observed to experience excess runoff and flash-flooding. Additionally, these conditions triggered landslides and debris flows through the reactivation of coseismic landslides. The *R* field (Fig. 4d) is used to represent the local mean values of a log-normal distribution assumed at each grid cell. Section 5.2. through 5.4 use this map as forcing in the Monte Carlo solutions (Equations 2 and 6).

5.2 Landslide hazard model confirmation for the March 15 AR

Before we present the regional model, a brief model confirmation is developed for the March-15 AR event, using the receiver operating characteristic (ROC) curves (Fawcett, 2006) at the Askerhan and Tut validation sites (Fig. 2). In the Askerhan catchment (Fig. 5), dBSI-identified landslides aligned well with strong ground motion, with 74% occurring in areas of >0.6 g PGA, closely matching the 78% of coseismic inventory points within the same PGA criteria. The dBSI points

https://doi.org/10.5194/egusphere-2025-3011
Preprint. Discussion started: 1 July 2025

in this catchment had a lower median slope (23°) than the observed coseismic inventory (29°), suggesting potential inclusion of rainfall-induced post-seismic failures. In the Tut validation area, landslide points captured by dBSI expressed median slope of 31° compared to the field study coseismic landslide inventory median slopes of 30°. These results demonstrate consistency in the slope distributions between the field-mapped and dBSI-classified landslides, which were considered sufficient for use as a model test data set.

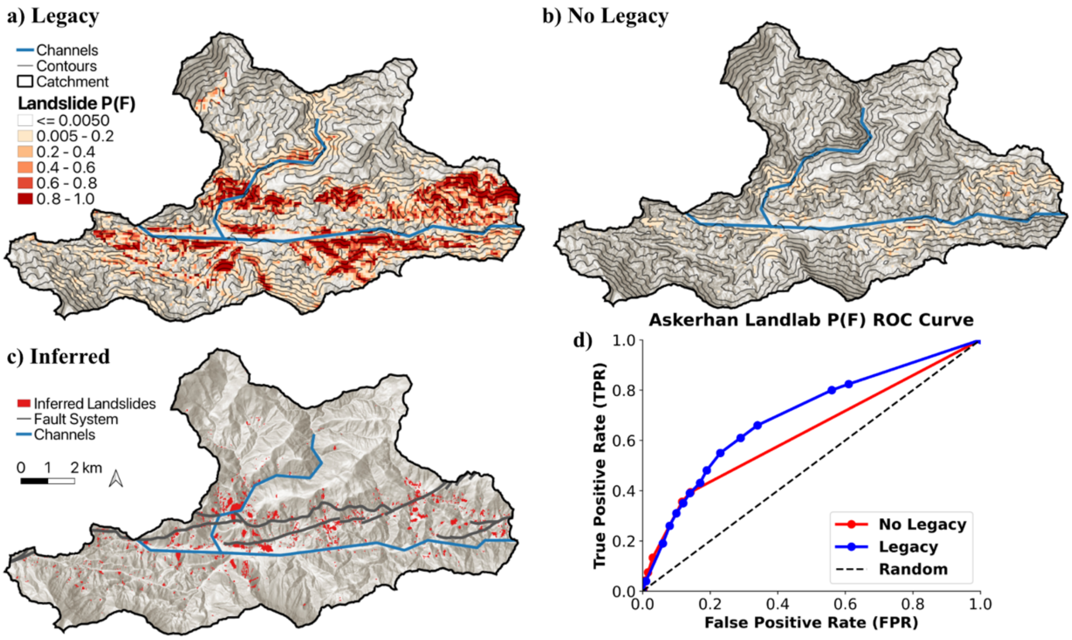

Figure 5. Illustration of model performance in the Askerhan subcatchment (see Fig. 2 for location). Modeled P(F): (a) with introduced earthquake legacy, (b) without legacy effects. (c) Inferred landslide inventory derived from dBSI algorithm presented in Ariza et al. (2021). (d) ROC curve based on the confusion matrix of the comparison between our observed landslide inventory and modeled Landlab predictions at varying thresholds. Legacy and non-legacy scenario AUC values are observed to be 0.70 and 0.63, respectively. Contours are at 100 m.

Mapped landslides and the modeled probability of the failure P(F) driven by the March 14-15 AR event are shown for the Askerhan subcatchment (Fig 5). Mapped landslides are largely concentrated on the northern flank of the watershed, separated by a channel. While the non-legacy model achieves modest ROC performance (True Positive Rate (TPR) = 0.39, False Positive Rate (FPR) = 0.14 in Askerhan; TPR = 0.64, FPR = 0.15 in Tut), its best thresholds are unrealistically low (P(F) = 0.001). A best threshold of P(F) = 0.001 suggests that to optimize model performance, we must highlight cells where failure is predicted in only 0.1% of simulations, which is a very low bar that reflects systematic underprediction by the model. The legacy model performs best at more physically meaningful thresholds (P(F) = 0.20), with higher detection rates at those thresholds (TPR = 0.55, FPR = 0.23 in Askerhan; TPR = 0.73, FPR = 0.24 in Tut), supporting the relevance of antecedent weakening.

With legacy effects incorporated, AUC values for Landlab ranged between 0.70 (Askerhan) and 0.80 (Tut), consistently outperforming the non-legacy scenario (0.63 and 0.76 for these subcatchments, respectively). Considering that the optimal P(F) thresholds for the best legacy model were significantly higher than that of the non-legacy model, our results indicate that earthquake legacy effects enhance the model's ability to predict landslide hazard with more realistic hazard estimates. In addition, modeled unstable areas often exceed observed landslides when calibrated with limited data (Sidle and Ochiai, 2006; Baum et al., 2010), but this should not be seen as overrepresentation, since the absence of mapped landslides doesn't rule out future landslides (Borga et al., 2002), despite appearing stable at the time of the inventory. These areas can highlight sites for further investigation of missed landslides or impending failures, including terrain that may be potentially unstable when exposed to storms of similar magnitude to the March 2023 AR event.

5.3 Regional landslide hazards of the March 14-15 Atmospheric River

In modeling secondary earthquake landslide hazards, introducing the earthquake legacy effects to model parameters is critical. In our model, a simple first-order approach is implemented based on observational evidence from the literature. The legacy effect approximation we used (Eq. 3), gives a range of total cohesion loss between 67% ($PGA = 0.75$) and 52.2% ($PGA = 0.15$) from the original pre-seismic parameters of the triangular distribution for total cohesion. Earthquake legacy leads to marked differences in the extent and magnitude of landslide probability for the March 14-15 AR event at the regional scale. Without the legacy effect, only a small portion of the landscape in steep slope areas (median $S > 40^{\circ}$) exhibit an increased landslide probability (e.g., P(F) > 0.2) during this AR event (Fig. 6b, c). A limited landslide response that is particularly concentrated in steep areas with thin topsoil layers that experience chronic instability, is expected from a storm with a greater than 5-year return period. However, when earthquake legacy is introduced, roughly 12% of the landscape (at slopes > 15º) exhibits P(F) > 0.2 (Fig. 6a, c). When incorporating legacy effects into the model, landslide hazard becomes particularly concentrated along the ruptured fault line from Tut to Askerhan and the badlands in the northeastern corner of the study area.

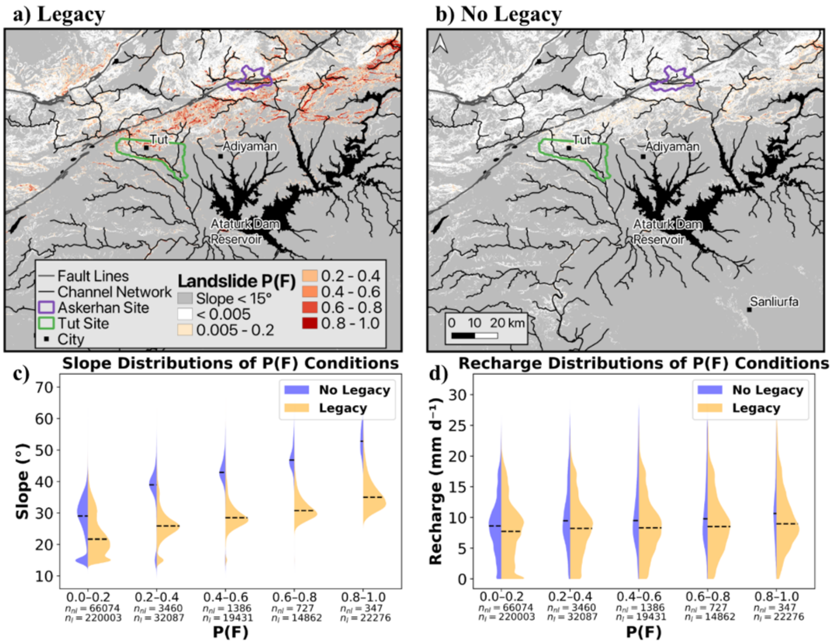

Figure 6. Landslide probability of failure P(F) maps for the central earthquake-impacted area overlain with mapped channel network: (a) with PGA-dependent legacy effect (Eq. 2) and (b) without legacy effects. (c, d) comparison of (a) and (b) using violin plots of local slopes and daily *R*, respectively, for different bins of landslide probabilities, excluding areas of P(F) = 0.

We illustrate the effects of earthquake legacy on slope stability for the March 15 AR event by comparing the slope distribution of potentially unstable cells within landslide probability bins (Fig. 6c). Overall, incorporating the legacy effects increases the number of cells with P(F) > 0 by 329%. In the non-legacy model run, ~92% of the potentially unstable cells are within the low P(F) values (P(F) ≤ 0.2). As the P(F) bin range increases, the influence of legacy effects on critical slope becomes more pronounced, with the largest difference (17.8°) observed at 0.8 < P(F) ≤ 1.0. On average, the difference in median slope is 13.3°, highlighting a consistent trend of a reduced critical slope angle for the legacy condition. The proportion of legacy cells also increases in higher P(F) bins, reflecting a shift in the likelihood of landsliding with respect to P(F), further supporting the role of legacy effects in shaping slope stability. The observed ~13° reduction in median critical slope for landslide initiation can have significant implications for hazard assessment and risk mitigation strategies.

Across bins where P(F) > 0.2, the median R required for potential failure in the legacy condition is an average of 1.2 mm d^{-1} lower than in the non-legacy scenario. This indicates that while earthquake legacy does slightly reduce the recharge threshold for landsliding, the effect is not as pronounced as the ~13° reduction in critical slope. This subtle difference can be due to a more uniform distribution of recharge rates across the landscape within the swath of the AR event. The contribution of recharge would have been more pronounced on the critical recharge rate solved for a given slope.

5.4 Landslide hazards under compound drivers

Existing landslide hazard assessment tools designed for global applications typically focus on seismic and rainfall drivers separately. In this section, we examine how landslide hazards change when these drivers are analyzed separately and in combination. Additionally, we compare the results to potential landslide hazards predicted for the March 14-15 AR event with post-seismic legacy conditions (Fig 6a).

We develop two additional coseismic landslide model runs with seismic drivers acting on (a) dry soils, which provide some baseline landslide response of the landscape to seismic activity when the soils are dry (Fig. 7a); and (b) wet soils, which uses recharge conditions for the March 14-15 AR event (Fig. 7b). These runs use P(F) from equation (6). Slope distributions for each scenario for different P(F) bins are shown in Fig. (7c).

Although there may be some control of soil saturation on landslide initiation during the Feb. 6, 2023 seismic activity, here we evaluate model performance under dry soil conditions to establish a baseline for coseismic hazard prediction across the whole study domain. Using the mapped landslide inventory from Görüm et al. (2023), we compare modeled probability of failure to ~12,000 grid cells representing 2,385 observed landslides. We limited our performance assessment to observed points with slope ≥ 15° in an attempt to filter out transition and deposition zones. To avoid bias from class imbalance, we sample an equal number of non-landslide cells (~12,000) for the ROC analysis. The dry soil model yields an AUC of 0.71, with an optimal P(F) threshold of 0.10 that produces a TPR of 0.53 and FPR of 0.15. This version of the model captures a substantial portion of the coseismic landslide signal with low false positive rates, supporting its use as a baseline for evaluating the compounding influence of legacy and hydrologic effects. However, its accuracy could likely be improved by incorporating realistic late-winter soil saturation levels typical of the region.

Interestingly, in all model simulations the low susceptibility region (defined by $P(F) \leq 0.2$ for this study) shows nearly identical distribution of local slopes, and similar median slope values (Fig. 7c). These stable areas are primarily located between the Mw 7.5 and 7.8 fault ruptures, where landslide initiation is limited regardless of the model conditions, likely reflecting comparatively moderate ground shaking and the presence of stronger rock types such as metamorphic, plutonic, and volcanic units. At high landslide susceptibility ($P(F) > 0.6$), a spatial comparison reveals that the number of cells increases in the following order: dry coseismic < legacy < wet coseismic (AR-before-EQ). This highlights that under saturated conditions, strong ground shaking from the earthquakes remains a dominant trigger for landsliding, even more so than post-seismic legacy effects.

At $P(F) > 0.2$, both dry coseismic and wet coseismic scenarios show bimodal slope distributions. The low slope peak is especially pronounced in the wet coseismic scenario, partially reflecting the influence of soil saturation resulting from the recharge of the AR event. However, the presence of this low slope peak even in the dry coseismic case, where no recharge is introduced, highlights the contribution of PGA to landslide initiation on gentle terrain. Meanwhile, the second peak in both models shifts towards steeper slopes at higher P(F) bins, indicating greater landslide susceptibility at steeper slopes.

In contrast, the legacy scenario displays a single dominant peak in the slope distribution with its median value increasing at higher P(F) bins. This unimodal behavior implies slope is a more direct control on P(F), potentially due to widespread cohesion weakening that reduces the failure threshold on already steep terrain, without generating a strong landslide susceptibility response in low-slope areas.

When comparing the dry coseismic and legacy models, while the dry coseismic model consistently predicts lower median critical slopes, it also has fewer cells at the highest probability range ($P(F) > 0.8$) and a greater number of cells in the moderate hazard range ($0.2 < P(F) \leq 0.6$). This suggests that the dry soil coseismic model identifies more widespread areas with moderate landslide potential, whereas the legacy model predicts more concentrated locations with higher landslide hazard.

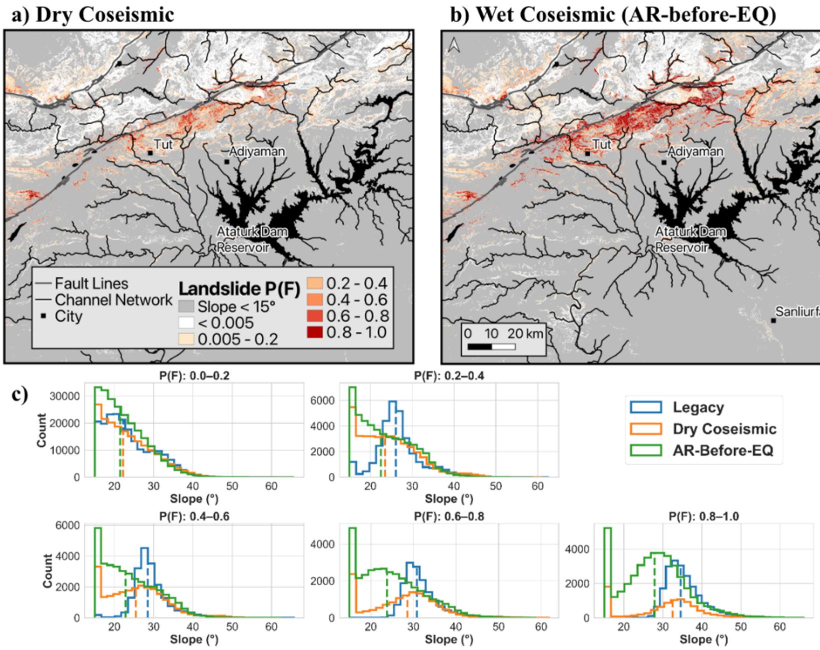

Figure 7. Landslide probability of failure P(F) maps for the central earthquake impacted area overlain with mapped channel network: for (a) coseismic-dry (no recharge) and (b) coseismic-wet, with recharge conditions of the March 15 AR event. (c) Histogram comparison of (a), (b), and the legacy model (Fig. 6a) using local slopes for different bins of P(F), excluding areas of P(F) = 0. Both Fig. 6a and Fig. 7b use R from the March 14-15, 2023 AR event.

5.5 Postseismic landslide hazard mapped from satellite records of extreme events

In this section, we evaluate how effectively combining historical climatology with earthquake legacy effects captures rainfall-driven landslide hazards for rapid analysis. Using the previous results as a baseline, we discuss how this approach can simulate soil saturation and landslide response without the need for real-time climate data. Weibull exceedance probability is used over the IMERG catalog, which provided daily rainfall from June 1, 2000 to March 31, 2024, to determine the return period of annual maximum rainfall over the study domain (Makkonen et al., 2006; Fig. 8a). Extreme events in this region are often more spatially localized due to AR processes (Gorum et al., 2025). To detect the annual maximum rainfall in the historical data, we used a time series of spatial maxima of daily IMERG rainfall across the domain, as opposed to using spatially averaged daily rainfall.

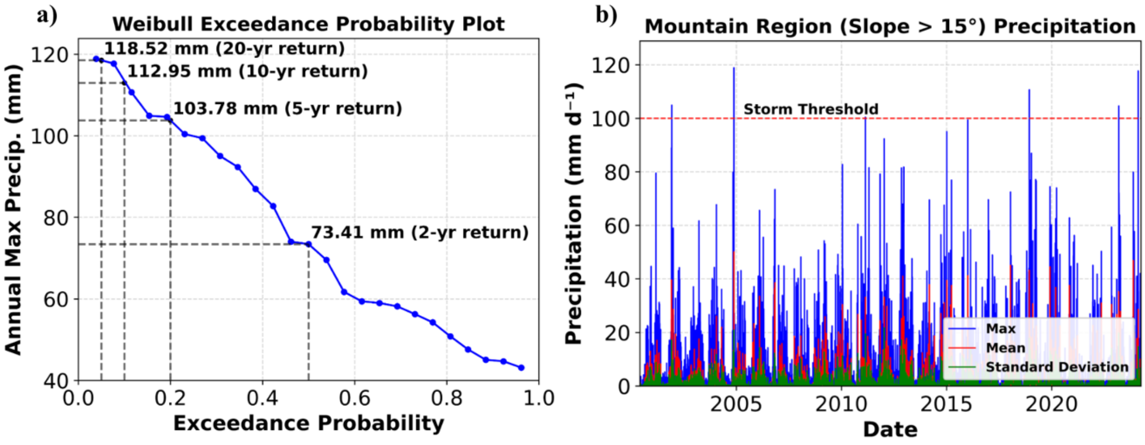

Figure 8. (a) Weibull exceedance probability plot for estimating return periods of extreme rainfall typical to the central earthquake impacted area domain. Standard Weibull plotting formula $P = \frac{m}{N+1}$ is used to determine plotting position where m and N correspond to rank order and number of samples, respectively. (b) The IMERG version 7 rainfall time series used to plot exceedance probability in (a) shows the average, maximum, and standard deviation of observed precipitation within the study domain.

We apply a threshold of 100 mm of daily rainfall as an indicator of an extreme event based on the 5-year return period level of rainfall (Fig. 8b). Four historical extreme precipitation events, excluding the March 14-15, 2023 event, are identified and the soil moisture model is run for each event for the 7-day window described in Section 3. Examples of the varying spatial distribution of cumulative 7-day rainfall and the compound max upslope average recharge rate fields are shown in Fig. 9.

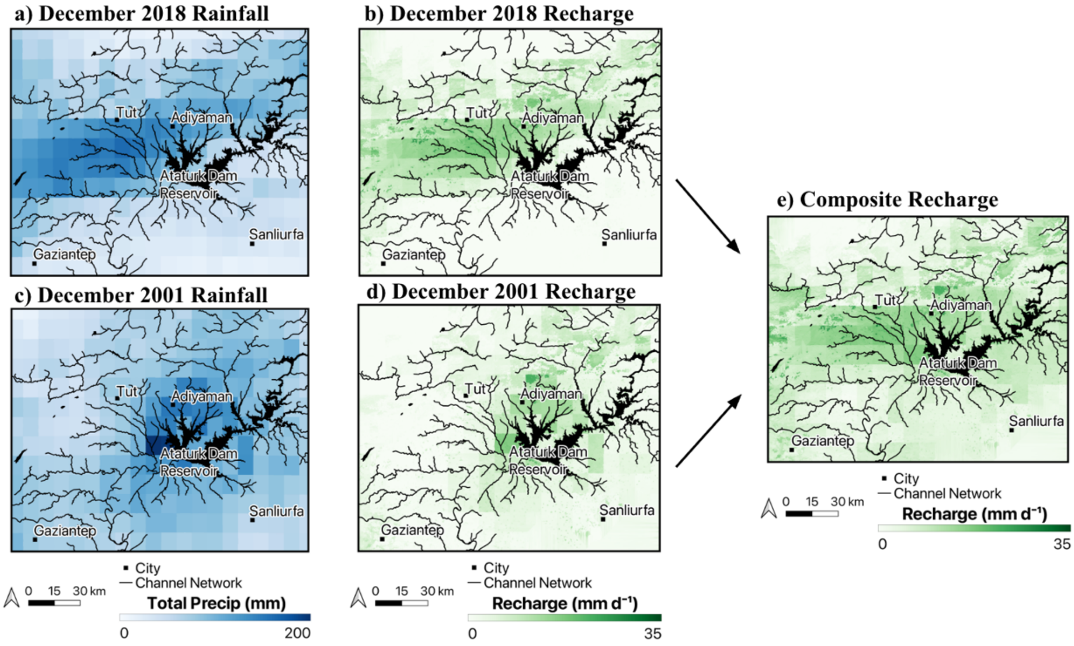

Figure 9. Cumulative rainfall and compound local maximum upslope average recharge for: (a, b) December 2018 and (c, d) December 2001 rainfall events; and (e) the composite recharge rate field of the combined pre-March 2023 extreme events identified in the IMERG catalog. Max daily recharge rate fields are derived from reduction processes outlined in Section 3.2. and are representative of the maximum daily recharge observed over the 7-day period for each cell.

To create a historical maximum upslope averaged recharge (R) field, we combine the max R fields from four extreme precipitation events by selecting the maximum daily recharge rate for each cell across all events. This composite map highlights areas with higher recharge and saturation levels during extreme rainfall. Both the event-specific (Fig. 4e) and historical rainfall (Fig. 9e) driven recharge rate fields report values concentrated in the Tut and Askerhan-Çelikhan region, the Burmapinar watershed and adjacent area north of the Ataturk Dam Reservoir, as well as the northeastern badlands. Notably, the historically driven recharge model reports higher spatial average (6.7 mm d^{-1} compared to 5.7 mm d^{-1}) and spatial maxima (32.8 mm d^{-1} compared to 26.7 mm d^{-1}) than the March 14-15 AR event.

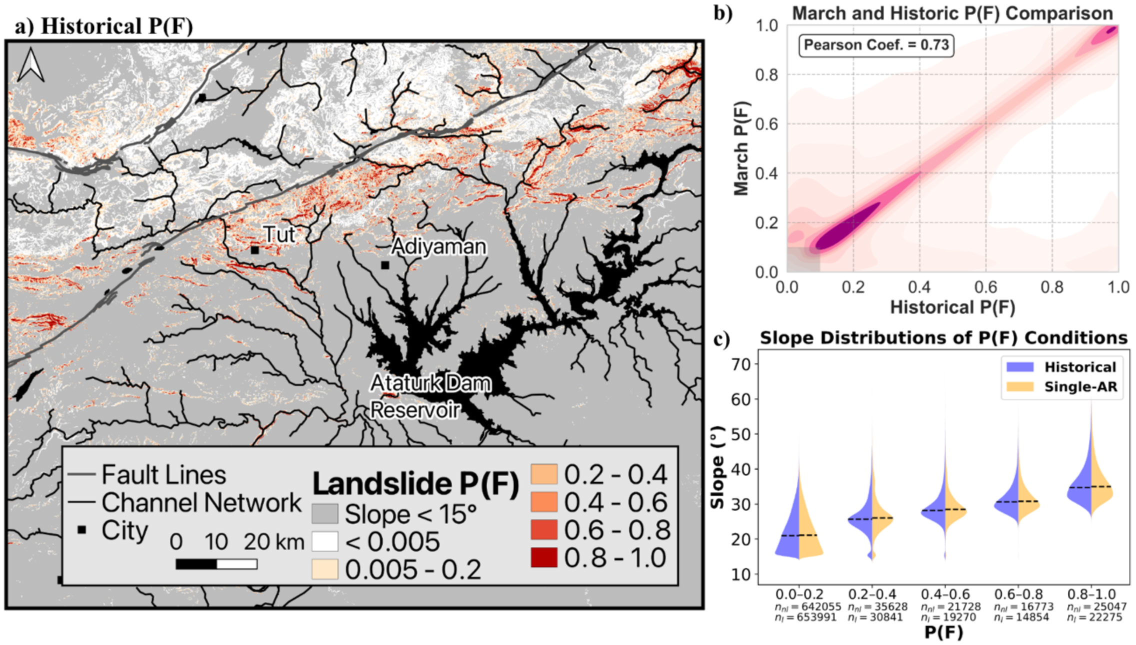

Figure 10. (a) P(F) map for the central earthquake-impacted area overlain with mapped channel network for simulations with PGA-dependent legacy effect (Eq. 6) and historical IMERG data driving the local recharge. (b) Kernel density estimation of March 2023 and historical model P(F), which visualizes the one-to-one cell comparison between the two models P(F) predictions. This comparison excludes generally stable cells (P(F) < 0.2 in both models) to highlight point cloud density at areas where we may realistically see landsliding. These omitted cells are represented by the gray box. Cells with legacy P(F) < 0.005 were excluded to evaluate how well the historic model reproduces areas of elevated hazard in the legacy scenario. (c) comparison of March 2023 and historical rainfall-driven model using violin plots of local slopes for different bins of P(F).

The historical P(F) obtained using the compound recharge map aligns well with the P(F) of March 14-15, 2023 AR event (Fig. 10a). Both models highlight risk in areas prone to landsliding (Fig. 6a, 10a), such as high drainage zones and steep barren slopes, particularly in the Burmapinar watershed and the town of Tut which saw catastrophic damage (Görüm et al., 2023). To compare the consistency of the historical and single-AR scenarios at the cellular level, we compare the prediction point cloud density using a kernel density estimation (Fig. 10b). Since landsliding is a rare occurrence that is spatially limited in a large region, we apply a 15° slope filter and a low probability threshold (P(F) ≤ 0.2) to exclude areas where landsliding risk is low. This comparison reveals a strong one-to-one correlation between the two models at the grid-cell level (Pearson Coefficient = 0.73), further confirming the two methods' consistency in identifying high-risk areas not only at the same spatial proportions, but at similar points in space. This agreement is reinforced by the slope distributions within each P(F) bin (Fig. 10c): violin plots show nearly identical distributions between the historical and single-AR scenarios, with median critical slopes varying by no more than 0.4°, suggesting the models converge on similar thresholds for failure across the landscape. The consistency of the legacy and historical models demonstrates that hazard maps based on historical rainfall extremes can serve as reliable proxies for real-time forecasts, offering a practical and proactive tool for anticipating post-seismic landslide risk in advance of future storm events.

6. Discussion and conclusions

We have developed a regional model of probabilistic shallow landsliding based on the infinite-slope stability equation, driven by peak ground acceleration and rainfall. Earthquake legacy is parameterized empirically to reduce a combined cohesion parameter for post-seismic rainfall applications. Model uncertainty is accounted for through the use of stochastic model parameters in a Monte Carlo simulation.

Infinite slope stability models are best suited for shallow landslide failures (Gong et al., 2023), and are generally not appropriate for deep-seated bedrock landslides, particularly where pre-existing discontinuities (e.g., faults, joints, bedding planes) control failure (Barton and Choubey, 1977; Hoek and Brown, 2019). However, at regional scales, it is impractical to characterize landslide type, failure surface geometry, or material type in detail. As a result, Mohr-Coulomb strength parameters and infinite slope stability analyses remain widely applied in regional, physically based models (e.g., Gallen et al., 2017; Jibson et al., 2000). To parameterize our model, we assigned cohesion and friction angle values based on lithologic units using values reported for the Himalayan region (Xi et al., 2024). We found that using only root cohesion values systematically overestimated P(F). Incorporating rock-derived cohesion reduced this bias and better reflected the mixed soil–rock conditions of the study area.

Landslide hazard models are generally developed for rainfall (Baum et al., 2010; Strauch et al., 2018; Alvarado-Franco et al., 2017) and seismic (Jibson, 1993; Zang et al., 2020) drivers separately. This approach was arguably justified by model developers, as the underlying drivers and mechanisms are different and independent, and the likelihood of extreme seismic and storm events coinciding with each other is relatively low. In addition, hydrologic and seismic data has been limited, especially prior to the satellite era, which hampered the development of compound hazard models. Hydrologic observations of the critical zones shows that soil water, especially the subsurface flow, usually has a long residence time, and unless earthquakes happen during the dry season, seismic shaking will inevitably coincide with some form of soil water (Montgomery et al., 1997; Anderson et al., 1997). This has been recognized in geotechnical research in the development of liquefaction models for ground failure during earthquakes. Such models make assumptions of the role of soil water and the location of the water table to map liquefaction hazards (Holzer et al., 2008; Baise et al., 2006). Coseismic landslide hazard models, which generally use some form of Newmark analysis that incorporate PGA to the infinite slope stability equation, often neglect soil water or make spatially uniform assumptions, such as positioning a fixed depth of water table in the soil column, to develop alternative scenarios (Shao et al., 2022; Djukem et al., 2024).

In addition, earthquakes leave legacy on the hydrologic and geotechnical properties of hillslopes, which collectively increase the susceptibility of hillslopes to rainfall-driven landslide hazards. This effect is similar to the effects of wildfires in watersheds, where root decay and heat affected changes in soil hydraulic properties elevate landslide risk until vegetation growth and soil recovery restore slope stability (Wells, 1987; Wondzell and King, 2003; Rengers et al., 2020). However, unlike post-wildfire behavior, our understanding of seismic legacy effects impact on slopes and the associated recovery remains limited. This phenomenon has received relatively little attention in the literature, particularly with respect to characterization through landslide observations and slope stability analysis (Xi et al., 2024; He et al., 2023; Brain et al., 2021; Leshchinsky et al., 2021). Recent observations of the compound landslide hazards following the February 6, 2023 Türkiye–Syria earthquake demonstrate how multiple triggering factors (e.g., strong ground shaking, elevated soil moisture, and subsequent extreme rainfall) can co-occur and be directly observed through a combination remote-sensing and gauge data (Görüm et al., 2025). Antecedent warming that lead to increased snowmelt elevated soil moisture to nearly the 95th percentile of February conditions, and the March 14–15 AR then pushed soil moisture above the 95th percentile for March (Görüm et al., 2025). In addition, empirical relationships suggest that slope shear strength may have been reduced by as much as 52–77% in certain areas following the February 6 earthquakes, due to the intensity of ground shaking (Xi et al., 2024; Görüm et al., 2025). When intense rainfall fell on these seismically compromised slopes, it was observed to have reactivated coseismic deposits and triggered widespread debris flows (Görüm et al., 2025).

Due to the limited amount of major earthquakes and coseismic landslide observations, and an influx of high-resolution global datasets from satellites, many susceptibility studies rely on machine-learning frameworks that focus on correlations, or predictive power, of input variables rather than physical explanation (Maurer et al., 2023). For example, some of these models use fault-distance metrics as a proxy for earthquake legacy effects, while others rely on hydrologic data at the landscape-level (e.g. rainfall, soil moisture, or streamflow) as the driving hydrologic input instead of simulating infiltration (Shahabi et al., 2015; Youssef et al., 2023; Fan et al., 2020). Due to the scarcity of detailed global hydrologic data that is publicly accessible, some post-earthquake methodologies omit hydrologic inputs entirely (Chen et al., 2020). Moreover, AI-driven geohazard models frequently demand large training datasets, risk overfitting, and lack transparency (Maurer et al., 2023). By linking geologic and hydrologic within a single mechanistic framework, and using a reduction in shear strength (RSS) parameterization to represent earthquake legacy, our model overcomes key gaps in existing susceptibility approaches and, together with recent work by Xi et al. (2024), offers a pathway for rainfall-driven landslide models to account for seismic effects. In validation, inclusion of earthquake legacy improved landslide detection rates and increased AUC at both study sites, while observing a reduction in the median critical slope for failure by approximately 13°, indicating that slopes deemed stable pre-earthquake may become highly susceptible afterward. This pronounced effect suggests that pre-seismic hazard maps likely underestimate post-earthquake risk, highlighting the need to update susceptibility analysis following major seismic events.

Validation of our model predictions in two subcatchments that exhibited high post-seismic landslide activity demonstrated considerable accuracy at identifying landslide hazard, although further investigation with calibration of model parameters to

https://doi.org/10.5194/egusphere-2025-3011
Preprint. Discussion started: 1 July 2025

finer resolutions is recommended for higher precision of hazard predictions in these localized areas. This approach demonstrates the following points:

- Incorporating earthquake legacy effects improves landslide prediction accuracy at our validation sites for post-seismic rainfall-driven landslides. The legacy model achieves higher detection rates and improves AUC at both sites. Our approach suggests that existing rainfall-driven landslide hazard models can be updated for post-seismic periods with parsimonious parameterizations of earthquake legacy.

- Across the full study domain, the dry coseismic model yields AUC = 0.71 (TPR = 0.53, FPR = 0.15 at P(F) = 0.10). The model's conservative performance reflects dry antecedent conditions and provides a baseline for evaluating added effects of legacy and hydrologic forcing. Accuracy could likely be improved by calibrating soil saturation to February conditions typical to the area.

- Incorporating earthquake legacy effects leads to a ~13° reduction in median critical slope for landslide initiation compared to the non-legacy model, indicating that slopes considered stable before an earthquake may become highly susceptible afterward. This suggests that pre-earthquake hazard maps may significantly underestimate post-earthquake risk, reinforcing the need to update susceptibility assessments following major seismic events.

- The scenario where the AR event precedes the earthquakes shows the greatest landslide hazard, with median critical slopes up to 7° lower than other models in high-probability bins (P(F) > 0.6) and nearly double the number of grid cells exceeding P(F) > 0.8 compared to the next closest model. This result points to a potentially important hazard scenario not seen in the historical record and highlights the need for more research on how the timing of storms and earthquakes influences landslide risk.

- Historical recharge patterns effectively predict landslide hazard with nearly identical spatial predictions and slope thresholds compared to models using data from the March 14–15, 2023 AR event. This demonstrates the potential for developing seasonal landslide outlooks in earthquake-impacted regions, allowing for early identification of high-risk areas before the onset of extreme rainfall.

It should be noted that validating hazard maps remains uncertain, particularly in remote mountainous regions where landslide inventories are often incomplete. An additional and more comprehensive evaluation of model performance would benefit from further field investigations to identify landslides or signs of instability that may have been missed in our satellite and mapping derived inventory.

Code and data availability

Components of Landlab, an open-source Python toolkit for two-dimensional numerical modeling of earth surface dynamics, used in this study are available at GitHub: http://github.com/landlab/landlab (Barnhart et al., 2020; Hobley et al., 2017). Documentation, installation instructions, and dependencies for Landlab can be found at http://landlab.github.io/. Full, annotated code detailing the application of Landlab in this project can be found at https://github.com/HunterJimenez by the time of publication.

Author contribution

Hunter N. Jimenez prepared the manuscript with contributions from all coauthors. Hunter N. Jimenez and Erkan Istanbulluoglu developed model code and performed simulations.

Competing interests

The authors declare that they have no conflict of interest.

Acknowledgements

This study was supported by the NASA Disasters Program grant number 80NSSC23K1103. T.G. and H.T. also acknowledge support from the NATO Science for Peace and Security Program (SPS project G6190).

References

Abbaszadeh, M., Shahriar, K., Sharifzadeh, M., and Heydari, M.: Uncertainty and reliability analysis applied to slope stability: a case study from Sungun copper mine, Geotechnical and Geological Engineering, 29, 581–596, doi:10.1007/s10706-011-9405-1, 2011.

Alvarado-Franco, J.P., Castro, D., Estrada, N., Caicedo, B., Sánchez-Silva, M., Camacho, L.A., Muñoz, F.: Quantitative-mechanistic model for assessing landslide probability and pipeline failure probability due to landslides, Eng Geol 222:212–224, doi: 10.1016/j.enggeo.2017.04.005, 2017.

Anderson S.P., Dietrich W.E., Montgomery D.R., Torres R., Conrad M.E., Loague K.: Subsurface flow paths in a steep, unchanneled catchment, Water Resources Research 33: 2637–2653, doi: 10.1029/97WR02595, 1997.

Ariza, A., Davila, N. A., Kemper, H., and Kemper, G.: LANDSLIDE DETECTION IN CENTRAL AMERICA USING THE DIFFERENTIAL BARE SOIL INDEX, Int. Arch. Photogram. Remote Sens. Spatial Inf. Sci., XLIII-B3-2021, 679–684, https://doi.org/10.5194/isprs-archives-XLIII-B3-2021-679-2021, 2021.

https://doi.org/10.5194/egusphere-2025-3011
Preprint. Discussion started: 1 July 2025

Assouline, S., and Or, D.: Anisotropy factor of saturated and unsaturated soils, Water Resour. Res., 42, W12403, doi:10.1029/2006WR005001, 2006.

Baise L.G., Higgins R.B., Brankman C.M.: Liquefaction hazard mapping—statistical and spatial characterization of susceptible units, J Geotech Geoenviron Eng, 132(6), 705–15, https://doi.org/10.1061/(ASCE)1090-0241(2006)132:6(70) , 2006.

Barnes, R., Lehman, C., Mulla, D.: Priority-flood: An optimal depression-filling and watershed-labeling algorithm for digital elevation models, Computers and Geosciences 62(C), 117 – 127, https://dx.doi.org/10.1016/j.cageo.2013.04.024, 2014.

Barnhart, K. R., Hutton, E. W. H., Tucker, G. E., Gasparini, N. M., Istanbulluoglu, E., Hobley, D. E. J., Lyons, N. J., Mouchene, M., Nudurupati, S. S., Adams, J. M., and Bandaragoda, C.: Short communication: Landlab v2.0: a software package for Earth surface dynamics, Earth Surf. Dynam., 8, 379–397, https://doi.org/10.5194/esurf-8-379-2020, 2020.

Barton, N., Choubey, V.: The shear strength of rock joints in theory and practice, Rock Mech. 10, 1–54, https://doi.org/10.1007/BF01261801, 1977.

Baum, R. L., W. Z. Savage, and J. W. Godt: TRIGRS—A FORTRAN program for transient rainfall infiltration and grid-based regional slope-stability analysis, U.S. Geol. Surv. Open File Rep. 02-0424, 64 pp, http://pubs.usgs.gov/of/2002/ofr-02-424/, 2002.

Baum, R. L., Godt, J. W., and Savage, W. Z.: Estimating the timing and location of shallow rainfall-induced landslides using a model for transient, unsaturated infiltration, J. Geophys. Res.-Earth, 115, F03013, https://doi.org/10.1029/2009JF001321, 2010.

Beven, K. J. and Kirkby, N. J.: A physically based variable contributing area model of basin hydrology, Hydrol. Sci. B., 24, 4369, https://doi.org/10.1080/02626667909491834, 1979.

Borga, M., Fontana, G. D., and Cazorzi, F.: Analysis of topographic and climatic control on rainfall-triggered shallow landsliding using a quasi-dynamic wetness index, J. Hydrol., 268, 56–71, https://doi.org/10.1016/S0022-1694(02)00118-X, 2002.

Bozkurt, D., Sen, O. L., Ezber, Y., Guan, B., Viale, M., Caglar, F.: Influence of African Atmospheric Rivers on Precipitation and Snowmelt in the Near East's Highlands, Journal of Geophysical Research: Atmospheres, 126, https://doi.org/10.1029/2020JD033646, 2021.

Brain, M. J., Rosser, N. J., and Tunstall, N.: The control of earthquake sequences on hillslope stability, Geophysical Research Letters, 44(2), 865–872, https://doi.org/10.1002/2016GL071879, 2017.

Brain, M. J., Moya, S., Kincey, M. E., Tunstall, N., Petley, D. N., and Sepúlveda, S. A.: Controls on Post-Seismic Landslide Behavior in Brittle Rocks, Journal of Geophysical Research: Earth Surface, 126(9), https://doi.org/10.1029/2021JF006242, 2021.

Burrows, K., Marc, O., and Andermann, C.: Retrieval of Monsoon Landslide Timings with Sentinel-1 Reveals the Effects of Earthquakes and Extreme Rainfall, Geophysical Research Letters, 50(16), https://doi.org/10.1029/2023GL104720, 2023.

Chen, W., Liu, L., Zhang, C., Wang, J., Wang, J., Pan, Y.: Monitoring the seasonal bare soil areas in Beijing using multi-temporal TM images, Int. Geosci. Remote Sens. Symp. 2004, 5, 3379–3382, doi: 10.1109/IGARSS.2004.1370429, 2004.

Chen, Y., Wei, Y., Wang, Q., Chen, F., Lu, C., and Lei, S.: Mapping Post-Earthquake Landslide Susceptibility: A U-Net Like Approach, Remote Sensing, 12(17), 2767, https://doi.org/10.3390/rs12172767, 2020.

Chen, Z., Huang, D., Wang, G.: A regional scale co-seismic landslide analysis framework: Integrating physics-based simulation with flexible sliding analysis, Eng. Geol. 2023 (315), 107040, doi: 10.1016/j.enggeo.2023.107040, 2023.

Dai, A., K. E. Trenberth, and T. R. Karl: Effects of Clouds, Soil Moisture, Precipitation, and Water Vapor on Diurnal Temperature Range, J. Climate, 12, 2451–2473, https://doi.org/10.1175/1520-0442(1999)012<2451:EOCSMP>2.0.CO;2, 1999.

Diek, S., Fornallaz, F., Schaepman, M.E., de Jong, R.: Barest Pixel Composite for agricultural areas using Landsat time series, Remote Sens. 2017, 9, 1245, https://doi.org/10.3390/rs9121245, 2017.

Djukem, D.L.W., Fan, X., Braun, A. et al.: Traditional and modified Newmark displacement methods after the 2022 Ms 6.8 Luding earthquake (Eastern Tibetan Plateau), Landslides 21, 807–828, https://doi.org/10.1007/s10346-023-02194-5, 2024.

Emre, Ö., Duman, T.Y., Özalp, S., Elmacı, H., Olgun, Ş., Şaroğlu, F.: Açıklamalı Türkiye diri fay haritası ölçek 1: 1.250. 000. Maden Tetkik ve Arama Genel Müdürlüğü, 2013.

Fan, X., Scaringi, G., Korup, O., West, A. J., van Westen, C. J., Tanyas, H., et al.: Earthquake-Induced Chains of Geologic Hazards: Patterns, Mechanisms, and Impacts, Reviews of Geophysics, 57(2), 421–503, https://doi.org/10.1029/2018RG000626, 2019.

Fan, X., Yunus, A. P., Scaringi, G., Catani, F., Siva Subramanian, S., Xu, Q., and Huang, R.: Rapidly evolving controls of landslides after a strong earthquake and implications for hazard assessments, Geophysical Research Letters, 48, e2020GL090509, https://doi.org/10.1029/2020GL090509, 2021.

Francis, O., Fan, X., Hales, T., Hobley, D., Xu, Q., and Huang, R.: The Fate of Sediment After a Large Earthquake, Journal of Geophysical Research: Earth Surface, 127(3), https://doi.org/10.1029/2021JF006352, 2022.

Fawcett, T.: An introduction to ROC analysis, Pattern Recogn. Lett., 27, 861–874, https://doi.org/10.1016/j.patrec.2005.10.010, 2006.

Gallen, S.F., Clark, M.K., Godt, J.W., Roback, K., Niemi, N.A.: Application and evaluation of a rapid response earthquake-triggered landslide model to the 25 April 2015 Mw 7.8 Gorkha earthquake, Nepal, Tectonophysics 714–715, 173–187, https://doi.org/10.1016/j.tecto.2016.10.031, 2017.

GDAL/OGR contributors: GDAL/OGR Geospatial Data Abstraction Software Library. Open-Source Geospatial Foundation. URL https://gdal.org DOI: 10.5281/zenodo.5884351, 2024.

Gong, W., Zekkos, D., Clark, M.: The influence of seismic displacement models on spatial prediction of regional earthquake-induced landslides, Eng. Geol. 325, 107288, https://doi.org/10.1016/j.enggeo.2023.107288, 2023.

Görüm, T., Tanyas, H., Karabacak, F., Yılmaz, A., Girgin, S., Allstadt, K. E., et al.: Preliminary documentation of coseismic ground failure triggered by the February 6, 2023 Türkiye earthquake sequence, Engineering Geology, 327, 107315, https://doi.org/https://doi.org/10.1016/j.enggeo.2023.107315, 2023.

Görüm, T., Bozkurt, D., Korup, O. et al.: The 2023 Türkiye-Syria earthquake disaster was exacerbated by an atmospheric river, Commun Earth Environ 6, 151, https://doi.org/10.1038/s43247-025-02111-9, 2025.

Hairong, D., Yong, L., Chongjian, S., Svirchev, L., Qiang, X., Zhaokun, Y., et al.: Mechanism of post-seismic floods after the Wenchuan earthquake in the upper Minjiang River, China, Journal of Earth System Science, 126(7), 96, https://doi.org/10.1007/s12040-017-0871-6, 2017.

Hammond, C., Hall, D., Miller, S., and Swetik, P. Level 1 stability analysis (LISA), documentation for Version 2.0. USDA, For. Serv., Moscow, ID, Intermountain Res. Sta. Gen. Tech. Rep. INT285, 1992.

He, K., Lombardo, L., Chang, L., Sadhasivam, N., Hu, X., Fang, Z. et al.: Investigating earthquake legacy effect on hillslope deformation using InSAR-derived time series, Earth Surface Processes and Landforms, 49(3), 980–990, https://doi.org/10.1002/esp.5746, 2024.

Hobley, D. E. J., Adams, J. M., Siddhartha Nudurupati, S., Hutton, E. W. H., Gasparini, N. M., Istanbulluoglu, E., and Tucker, G. E.: Creative computing with Landlab: An open-source toolkit for building, coupling, and exploring two-dimensional numerical models of Earth-surface dynamics, Earth Surface Dynamics, 5(1), https://doi.org/10.5194/esurf-5-21-2017, 2017.

Hoek, E., Brown, E.T.: The Hoek–Brown failure criterion and GSI–2018 edition, J. Rock Mech. Geotech. Eng. 11, 445–463, https://doi.org/10.1016/j. jrmge.2018.08.001, 2019.

Holzer, T.L., Noce, T.E., Bennett, M.J.: Liquefaction Hazard Maps for Three Earthquake Scenarios for the Communities of San Jose, Campbell, Cupertino, Los Altos, Los Gatos, Milpitas, Mountain View, Palo Alto, Santa Clara, Saratoga, and Sunnyvale, Northern Santa Clara County, California, U.S. Geological Survey Open-file Report 2008-1270, 29 p., 3 plates, and database [http://pubs.usgs.gov/of/2008/1270/], 2008.

Hovius, N., Meunier, P., Lin, C. W., Chen, H., Chen, Y. G., Dadson, S., et al.: Prolonged seismically induced erosion and the mass balance of a large earthquake, Earth and Planetary Science Letters, 304(3–4), 347–355, https://doi.org/10.1016/J.EPSL.2011.02.005, 2011.

Huang, R., and Fan, X.: The landslide story, Nature Geoscience, 6(5), 325–326, https://doi.org/10.1038/ngeo1806, 2013.

Jibson, R.W.: Predicting earthquake-induced landslide displacements using Newmark's sliding block analysis, Transportation Research Record, no. 1411, p. 9-17, 1993.

Jibson, R.W., Harp, E.L., Michael, J.A.: A method for producing digital probabilistic seismic landslide hazard maps. Eng. Geol. 58, 271–289, https://doi. org/10.1016/S0013-7952(00)00039-9, 2000.

Jones, J. N., Boulton, S. J., Stokes, M., Bennett, G. L., and Whitworth, M. R. Z.: 30-year record of Himalaya mass-wasting reveals landscape perturbations by extreme events, Nature Communications, 12(1), 6701, https://doi.org/10.1038/s41467-021-26964-8, 2021.

Kincey, M. E., Rosser, N. J., Densmore, A. L., Robinson, T. R., Shrestha, R., Singh Pujara, D., et al.: Modelling post-earthquake cascading hazards: Changing patterns of landslide runout following the 2015 Gorkha earthquake, Nepal, Earth Surface Processes and Landforms, 48(3), 537–554, https://doi.org/10.1002/esp.5501, 2023.

Laio, F., Porporato, A., Ridolfi, L., and Rodriguez-Iturbe, I.: Plants in water-controlled ecosystems: active role in hydrologic processes and response to water stress: II, Probabilistic soil moisture dynamics. Advances in Water Resources, 24(7), 707-723, https://doi.org/10.1016/S0309-1708(01)00005-7, 2001.

Lenti, L., and Martino, S.: A Parametric Numerical Study of the Interaction between Seismic Waves and Landslides for the Evaluation of the Susceptibility to Seismically Induced Displacements, Bulletin of the Seismological Society of America, 103(1), 33–56, https://doi.org/10.1785/0120120019, 2013.

Lepore, C., Arnone, E., Noto, L. V., Sivandran, G., and Bras, R. L.: Physically based modeling of rainfall-triggered landslides: a case study in the Luquillo forest, Puerto Rico, Hydrol. Earth Syst. Sci., 17, 3371–3387, https://doi.org/10.5194/hess-17-3371-2013, 2013.

Leshchinsky, B., Lehmann, P., and Or, D.: Enhanced Rainfall-Induced Shallow Landslide Activity Following Seismic Disturbance—From Triggering to Healing, Journal of Geophysical Research: Earth Surface, 126(1), e2020JF005669, https://doi.org/https://doi.org/10.1029/2020JF005669, 2021.

Lim, K. J., Engel, B. A., Muthukrishnan, S., and Harbor, J.: EFFECTS OF INITIAL ABSTRACTION AND URBANIZATION ON ESTIMATED RUNOFF USING CN TECHNOLOGY 1, JAWRA J. Am. Water Resour. Assoc., vol. 42, no. 3, pp. 629–643, Jun. 2006, doi: 10.1111/j.1752-1688.2006.tb04481.x, 2006.

Lin, C. W., Shieh, C. L., Yuan, B. D., Shieh, Y. C., Liu, S. H., and Lee, S. Y.: Impact of Chi-Chi earthquake on the occurrence of landslides and debris flows: Example from the Chenyulan River watershed, Nantou, Taiwan. Engineering Geology, 71(1–2), 49–6, https://doi.org/10.1016/S0013-7952(03)00125-X, 2004.

Liu, F., and Yang, S.: The effect of the Wenchuan earthquake on the fluvial morphology in the Longmen Shan, eastern Tibetan Plateau: Discussion and speculation. Quaternary International, 371, 280–289, https://doi.org/10.1016/j.quaint.2014.09.021, 2015.

Malkawi, A. I. H., Hassan, W. F., and Abdulla, F. A.: Uncertainty and reliability analysis applied to slope stability, Struct. Saf., 22, 161–187, https://doi.org/10.1016/S0167-4730(00)00006-0, 2000.

Makkonen, L.: Plotting Positions in Extreme Value Analysis, J. Appl. Meteor. Climatol., 45, 334–340, https://doi.org/10.1175/JAM2349.1, 2006.

Marc, O., Hovius, N., Meunier, P., Gorum, T., and Uchida, T.: A seismologically consistent expression for the total area and volume of earthquake-triggered landsliding, Journal of Geophysical Research: Earth Surface, 121(4), 640–663, https://doi.org/10.1002/2015JF003732, 2016.

Maurer, B. W., and Sanger, M. D.: Why "AI" models for predicting soil liquefaction have been ignored, plus some that shouldn't be, Earthquake Spectra, 39(3), 1883–1910, https://doi.org/10.1177/87552930231173711, 2023.

Meng, J., Kusky, T., Mooney, W. D., Bozkurt, E., Bodur, M. N., and Wang, L.: Surface deformations of the 6 February 2023 earthquake sequence, eastern Türkiye, Science (1979), vol. 383, no. 6680, pp. 298–305, doi: 10.1126/science.adj3770, 2023.

Meunier, P., Hovius, N., and Haines, J. A.: Topographic site effects and the location of earthquake induced landslides, Earth and Planetary Science Letters, 275(3–4), 221–232, https://doi.org/10.1016/j.epsl.2008.07.020, 2008.

Meunier, P., Uchida, T., and Hovius, N.: Landslide patterns reveal the sources of large earthquakes, Earth and Planetary Science Letters, 363, 27–33, https://doi.org/10.1016/J.EPSL.2012.12.018, 2013.

Montgomery, D. R., Dietrich, W. E., Torres, R., Anderson, S. P., Heffner, J. T., and Loague, K.: Hydrologic response of a steep, unchanneled valley to natural and applied rainfall, Water Resour. Res., 33, 91–109, https://doi.org/10.1029/96WR02985, 1997.

MTA. (2002). 1: 500,000 scaled Turkish geology map series. MTA Genel Mudurlugu, Ankara.

Newmark, N.M.: A Method of Computation for Structural Dynamics, Transactions, ASCE, Vol. 127, pp. 1406-1435, 1962.

Nudurupati, S. S., Istanbulluoglu, E., Tucker, G. E., Gasparini, N. M., Hobley, D. E. J., Hutton, E. W. H., et al.: On transient semi-arid ecosystem dynamics using Landlab: Vegetation shifts, topographic refugia, and response to climate, Water Resources Research, 59, e2021WR031179, https://doi.org/10.1029/2021WR031179, 2023.

Pack, R. T., Tarboton, D. G., and Goodwin, C. N.: The SINMAP approach to terrain stability mapping, in: Proceedings of the 8th international congress of the international association of engineering geology and the environment, Vancouver, British Columbia, Canada, 21–25 September, vol. 2, AA Balkema, Rotterdam, 1157–1165, 1998.

Pack, R. T., Tarboton, D. G., and Goodwin, C.: SINMAP 2.0-A Stability Index Approach to Terrain Stability Hazard Mapping, User's Manual, available at: https://digitalcommons.usu.edu/cgi/viewcontent.cgi?article=1015&context=cee_facpub (last access: 28 January 2018), 2005.

Rengers, F.K., McGuire, L.A., Oakley, N.S. et al.: Landslides after wildfire: initiation, magnitude, and mobility, Landslides 17, 2631–2641, https://doi.org/10.1007/s10346-020-01506-3, 2020.

Selby, M. J.: Hillslope Materials and Processes, 2nd Edn., Oxford University Press, Oxford, UK, 1993.

Shahabi, H., Hashim, M.: Landslide susceptibility mapping using GIS-based statistical models and Remote sensing data in tropical environments. Sci Rep 5, 9899, https://doi.org/10.1038/srep09899, 2015.

Shao, X., Xu, C.: Earthquake-induced landslides susceptibility assessment: a review of the state-of-the-art, Nat Hazards Res 2(3):172–182, https://doi.org/10.1016/j.nhres.2022.03.002, 2022.

Sidle, R. C. and Ochiai, H.: Landslides: processes, prediction, and land use, Water Resources Monogram 18, American Geophysical Union, Washington DC, 2006.

Steenhuis, T. S., Winchell, M., Rossing, J., Zollweg, J. A., and Walter, M. F.: SCS Runoff Equation Revisited for Variable-Source Runoff Areas, J. Irrig. Drain. Eng., 121, 234–238, https://doi.org/10.1061/(ASCE)0733-9437(1995)121:3(234), 1995.

Strauch, R., Istanbulluoglu, E., Nudurupati, S. S., Bandaragoda, C., Gasparini, N. M., and Tucker, G. E.: A hydroclimatological approach to predicting regional landslide probability using Landlab, Earth Surf. Dynam., 6, 49–75, https://doi.org/10.5194/esurf-6-49-2018, 2018.

Tanyaş, H., Kirschbaum, D., Görüm, T., van Westen, C. J., Tang, C., and Lombardo, L.: A closer look at factors governing landslide recovery time in post-seismic periods, Geomorphology, 391, 107912, https://doi.org/10.1016/J.GEOMORPH.2021.107912, 2021a.

Tanyaş, H., Kirschbaum, D., Görüm, T., van Westen, C. J., and Lombardo, L.: New Insight into Post-seismic Landslide Evolution Processes in the Tropics, Frontiers in Earth Science, 9, https://doi.org/10.3389/feart.2021.700546, 2021b.

U.S. Geological Survey, 2023a. M 7.5 - Elbistan earthquake, Kahramanmaras earthquake sequence, USGS Earthquake Hazards Program. [WWW Document]. URL https://earthquake.usgs.gov/earthquakes/eventpage/us6000jlqa.

U.S. Geological Survey, 2023b. M 7.8 - Pazarcik earthquake, Kahramanmaras earthquake sequence, USGS Earthquake Hazards Program. [WWW Document]. URL https://earthquake.usgs.gov/earthquakes/eventpage/us6000jllz.

van den Bout, B., Tang, C., van Westen, C., and Jetten, V.: Physically based modeling of co-seismic landslide, debris flow, and flood cascade, Nat. Hazards Earth Syst. Sci., 22, 3183–3209, https://doi.org/10.5194/nhess-22-3183-2022, 2022.

Wang, S., Ma, X., Zhou, S. et al.: Extreme atmospheric rivers in a warming climate, Nat Commun 14, 3219, https://doi.org/10.1038/s41467-023-38980-x, 2023.

Warner, M. D., Mass, C. F., and Salathé, E. P.: Changes in Winter Atmospheric Rivers along the North American West Coast in CMIP5 Climate Models, J. Hydrometeor., 16, 118–128, https://doi.org/10.1175/JHM-D-14-0080.1, 2015.

Wells II, W.G.: The effects of fire on the generation of debris flows in southern California, Debris Flows/Avalanches: Process, Recognition, and Mitigation, https://doi.org/10.1130/REG7-p105, 1987.

Wondzell, S.M., King, J.G.: Post-fire erosional processes in the Pacific Northwest and Rocky Mountain regions, Forest Ecology and Management 178, 75 – 87, https://doi.org/10.1016/S0378-1127(03)00054-9, 2003.

Wu, W. and Sidle, R. C.: A Distributed Slope Stability Model for Steep Forested Watersheds, Water Resour. Res., 31, 2097–2110, 1995.

Xi, C., Tanyas, H., Lombardo, L., He, K., Hu, X., and Jibson, R. W.: Estimating weakening on hillslopes caused by strong earthquakes, Communications Earth & Environment, 5(1), 81, https://doi.org/10.1038/s43247-024-01256-3, 2024.

Youssef, K., Shao, K., Moon, S. et al.: Landslide susceptibility modeling by interpretable neural network, Commun Earth Environ 4, 162, https://doi.org/10.1038/s43247-023-00806-5, 2023.

Zang, M., Qi, S., Zou, Y., Sheng, Z., and Zamora, B. S.: An improved method of Newmark analysis for mapping hazards of coseismic landslides, Nat. Hazards Earth Syst. Sci., 20, 713–726, https://doi.org/10.5194/nhess-20-713-2020, 2020.

Zhang, S., and Zhang, L. M.: Impact of the 2008 Wenchuan earthquake in China on subsequent long-term debris flow activities in the epicentral area, Geomorphology, 276, 86–103, https://doi.org/10.1016/j.geomorph.2016.10.009, 2017.